



저작자표시-비영리-변경금지 2.0 대한민국

이용자는 아래의 조건을 따르는 경우에 한하여 자유롭게

- 이 저작물을 복제, 배포, 전송, 전시, 공연 및 방송할 수 있습니다.

다음과 같은 조건을 따라야 합니다:



저작자표시. 귀하는 원저작자를 표시하여야 합니다.



비영리. 귀하는 이 저작물을 영리 목적으로 이용할 수 없습니다.



변경금지. 귀하는 이 저작물을 개작, 변형 또는 가공할 수 없습니다.

- 귀하는, 이 저작물의 재이용이나 배포의 경우, 이 저작물에 적용된 이용허락조건을 명확하게 나타내어야 합니다.
- 저작권자로부터 별도의 허가를 받으면 이러한 조건들은 적용되지 않습니다.

저작권법에 따른 이용자의 권리는 위의 내용에 의하여 영향을 받지 않습니다.

이것은 [이용허락규약\(Legal Code\)](#)을 이해하기 쉽게 요약한 것입니다.

[Disclaimer](#)

공학석사 학위논문

**Enhancement of
Mechanoluminescence Sensitivity of
 $\text{SrAl}_2\text{O}_4:\text{Eu}^{2+},\text{Dy}^{3+}$ Composite by
Ultrasonic Curing Method**

초음파 경화 법에 의한 $\text{SrAl}_2\text{O}_4 : \text{Eu}^{2+}, \text{Dy}^{3+}$
복합재료의 응력발광 감도 향상

2020 년 2 월

서울대학교 대학원

기계항공공학부

토마스 웨베 케레케스

**Enhancement of Mechanoluminescence Sensitivity of
SrAl₂O₄:Eu²⁺,Dy³⁺ Composite by Ultrasonic Curing
Method**

초음파 경화 법에 의한 SrAl₂O₄ : Eu²⁺, Dy³⁺
복합재료의 응력 발광 감도 향상

지도 교수 윤군진

이 논문을 공학석사 학위논문으로 제출함
2019 년 11 월

서울대학교 대학원
기계항공공학부
토마스 웨베 케레케스

토마스 웨베 케레케스의 공학석사 학위논문을
인준함
2019 년 12 월

위원장 김용협 (인)

부위원장 윤군진 (인)

위원 신상준 (인)

Abstract

Enhancement of Mechanoluminescence Sensitivity of SrAl₂O₄:Eu²⁺,Dy³⁺ Composite by Ultrasonic Curing Method

Tomas Webbe Kerekes

Department of Mechanical and Aerospace Engineering

The Graduate School

Seoul National University

In this thesis, we present a novel approach to enhance the mechanoluminescent (ML) sensitivity of composite made with epoxy resin and strontium aluminate co-doped with europium ions and dysprosium ions (SAOED) by subjecting it to ultrasonic vibration throughout the curing process. Four molds of epoxy/SAOED composite were subjected to different ultrasonic frequencies; 200 kHz; 120 kHz; 40 kHz and control 0 kHz. Tensile strain was applied to the cured specimens and their ML reaction was video recorded. The images were analyzed in order to obtain the light intensity (LI) variation for generating an ML light intensity change ratio (LICR) analysis and minimum measurable strain ML sensitivity evaluation. Scanning electron microscopy (SEM) was used to observe the interphase bonding differences of each sample and micro-computed tomography (micro-CT) test was conducted to

examine the particle dispersion in the composites. The results showed that applying ultrasonic vibration during the curing process increased the ML sensitivity of the composite by strengthening the interphase bonding.

Keywords: Strontium aluminate, mechanoluminescent, ultrasonic vibration, wettability, stress/strain sensor, epoxy/SAOED composite.

Student Number: 2017-24235

Table of content

1. INTRODUCTION.....	1
1.1. Background and motivation	1
1.2. Objectives and thesis overview	3
2. EXPERIMENTAL	4
2.1. Materials	4
2.2. Ultrasonic curing treatment (UCT) manufacturing procedures	6
2.3. ML sensitivity test setup and procedure.....	9
2.4. Minimum measurable strain test.....	1 2
2.5 SEM analysis and micro-CT test.....	1 3
2.6 Temperature-monitoring during ultrasonic curing	1 4
3. RESULTS AND DISCUSSIONS	1 7
3.1 ML sensitivity analysis.....	1 7
3.2 Minimum measurable strain analysis.....	2 1
3.3 Fractography for UCT Sonicated Interface Bonding with SEM.	2 2
3.3.1 Fractography after tensile test at room temperature.....	2 2
3.3.2 Fractography with slicing action.....	2 5
3.3.3 Fractography at cryogenic temperature	2 7

3.4 Dispersions of UCT epoxy/SAOED Composites by Micro Computed Tomography	3 0
3.4.1 Nearest Neighboring Distance	3 0
3.4.2 Quantitative Comparison According to the Ultrasonic Frequency	3 1
3.5 Physical Mechanisms of Interfacial Bonding Augmentation by UCT Method...	3 5
4. CONCLUSION AND FUTURE WORKS.....	3 7
4.1 Conclusion.....	3 7
4.2. Future Works.....	3 9
5. REFERENCES.....	4 0
6. APPENDICES.....	5 0
Appendix A. Experimental results	5 0
Appendix B. SEM images	5 8
Appendix D. Materials and equipment	7 6
Appendix C. UCT system assembly	8 5

List of figures

Figure 1. SEM images of SOAED powders. (a) M 27.09 μm (b) F 15.45 μm (c) FF 3.32 μm	4
Figure 2. Particle size distribution of SAOED particles.....	5
Figure 3. Mechanoluminescence of SAOED composites [90].....	6

Figure 4. (a) UCT setup. (b) Metal sheets-transducer assembly.	7
Figure 5. (a) Vacuum chamber and pump. (b) Impeller mixer for simultaneous degassing and mixing.	7
Figure 6. Schematic overview of epoxy/SAOED composite UCT manufacturing.	8
Figure 7. Dog-bone specimen dimensions.	9
Figure 8. (a) Complete ML sensitivity test setup. (b) ML sensitivity test setup without dark environment cover.	1 1
Figure 9. Image obtained during ML sensitivity test.	1 1
Figure 10. ML sensitivity test setup.	1 2
Figure 11. Image processing flow of raw image (a) → b) → c) → d) → e) → f) → g)).	1 4
Figure 12. Temperature-monitoring setup.	1 5
Figure 13. Temperature history profile graph of the 4 curing samples (3 thermocouples per sample).	1 6
Figure 14. M size SAOED particles average LICR values.	1 7
Figure 15. F size SAOED particles average LICR values.	1 8
Figure 16. FF size SAOED particles average LICR values.	1 8
Figure 17. Comparisons of ML sensitivity for different sonication frequencies and sizes.	1 9
Figure 18. SEM of the fractured cross section of M 27.09 μm particle size (a, b) 0 kHz, (c, d) 40 kHz, (e, f) 120 kHz and (g, h) 200 kHz.	2 4
Figure 19. SEM of the microtome machined samples. F 15.45 μm particle size. (a), (b) 0 kHz. (c), (d) 40 kHz. (e), (f) 120 kHz. (g), (h) 200 kHz.	2 7
Figure 20. SEM of the cryogenically treated samples F 15.45 μm particle size. (a), (b) 0 kHz; (c), (d) 40 kHz; (e), (f) 120 kHz; (g), (h) 200 kHz.	3 0
Figure 21. Schematics of the composites according to the ultrasonic frequency.	3 1
Figure 22. CDF distribution of the particle NND.	3 3
Figure 23. Probability Density Function of the Particle Surface Area and Volume.	3 4

List of tables

Table 1. Particle size analysis results of SAOED powder.....	5
Table 2. Max temperature and time reached	1 6
Table 3. Comparison of ML sensitivity for different frequencies and sizes.	1 9
Table 4. Particle size and minimal strain ML reaction.....	2 2
Table 5. Morphological Properties of the Particles in Composites.	3 2

1. Introduction

1.1. Background and motivation

$\text{SrAl}_2\text{O}_4:\text{Eu}^{2+}, \text{Dy}^{3+}$ (SAOED) was developed by Matsuzawa et al. in 1996 [1]. It is a green emitting phosphor with a long lasting and considerably bright phosphorescence [2]. SAOED is a persistent luminescent material (PLM) composed of strontium aluminate co-doped with lanthanide ions such as europium ion and dysprosium ion [3]. PLMs have developed into a relevant source of multi-functional materials with a wide range of applications in several fields [4-6]. It is well known that SAOED emits an intense light when it is subjected to elastic-plastic deformation or friction [7-10]. Moreover, the intense green light can be clearly observed by the naked eye in the atmosphere [11]. This characteristic has been successfully implemented as a sensing technique for structural health monitoring system capable of visualizing active cracks; crack propagation or stress concentration indicator [12-14]; impacts and friction [17]; compression and film pressure sensor [15, 16]. Recently, ML has attracted the attention of numerous researchers due to its potential application in diverse types of mechano-optical devices [17] and nondestructive evaluation [18-21]. Research has been carried out regarding the feasibility to implement SAOED in the visualization and measurement of stress distribution in solids. Significant progress has been made and diverse concepts were proposed regarding the technical implementation of SAOED as a stress and strain full field

nondestructive sensing tool such as epoxy/ML composite [7, 8, 22-26]; ML sensing film and adhesive ML lamina [5, 27-31]; ML coating sensor [9, 32, 33]; ML sensing paint [34, 35]; structural health monitoring crack propagation sensor and concrete fracture prediction ML sensor [36, 37]; stress detection through imaging of ML distribution [38] and compressed ML powder pellets [39].

Furthermore, researchers investigated several methods to enhance the LI, persistent luminescence (PL) and ML properties of SAOED and epoxy/SAOED composites in order to develop a high sensitivity ML sensor by means of swift heavy ion irradiation and co-doping [40-56]; combustion synthezation of submicron and nanosized SAOED powder [57, 58]; hollow microspheres preparation by using a solvothermal co-precipitation method [59] and electron beam bombardment (EBB) [60, 61]. However, there is no literature proposing the enhancement of the SAOED PL and/or ML properties by means of strengthening the interphase bonding between the SAOED particles and the matrix.

Previous studies reported that the increased wettability between the filler and matrix improves the integrated bonding of an interphase [62-69]. One way to achieve this is by lowering the interfacial tension between the matrix and fillers. As the surface tension of liquid in general higher than that of solid, increasing the surface tension of solid fillers generally helps improve wetting and adhesion. Modification of surface tension of fillers can be done by dry (gaseous) or wet oxidation [70, 71]; electrochemical methods [72-74]; plasma etching or grafting [75-79]; polymer coating [80, 81]; chemical treatment [82-85] or high-energy irradiation [86]. Other

researches attempted to improve the interfacial bonding by subjecting epoxy/carbon fiber and epoxy/aramid fiber composites to ultrasonic vibration [87-89]. While those studies implicated that sonication enhanced wettability by reducing the surface tension of the epoxy resin, this is not valid as the surface tension of a matter hardly changes at the constant temperature. Instead, the enhanced adhesion between the fillers and epoxy, in the presence of vibration, may be attributed to the increased surface area of fillers and epoxy with direct contact. The sonic vibration may help the pinning of viscous epoxy into the rough surface of particles, thus increasing the contact area between two phases. This phenomenon is the reason on which this thesis is based.

1.2. Objectives and thesis overview

This study proposes a novel approach to enhance the sensitivity of epoxy/SAOED composite by subjecting the composite to ultrasonic vibration throughout the curing process. In regards to the novel approach, we compared ML sensitivities and minimum measurable strains for different sonication frequencies. After evidencing clearly enhanced sensitivity attributed to the proposed manufacturing approach, various characterizations were conducted to explain the phenomenon. ML particles dispersions with different ultrasonic frequencies were characterized by micro-CT. The interfacial contact between epoxy and SAOED particles was SEM observed. It is anticipated that the finding of this research would contribute to the development of a super-sensitive ML stress/strain sensor composite capable of measuring small

strain values with high accuracy, with the enhanced sensitivity to elastic and plastic deformation.

2. Experimental

2.1. Materials

The ML composite was formulated with the weight ratio of 100 epoxy : 10 SAOED powder. The epoxy resin used was West System® 105 Epoxy Resin®/207 Special Clear Hardener™ (Gougeon Brothers, Inc.) The mixture of epoxy and hardener has a mix viscosity at 760 cps at 22.2°C when tested by ASTM D-2393. The cure-to-solid time is 10 to 15 hours and the cure-to-working strength time is 1 to 4 days. Three different sizes of SAOED were obtained from LumiNova® (Nemoto & Co., Ltd.). The particle size was analyzed by the laser diffraction method in accordance with ISO 13320 using LS 13 320 Particle Sizing Analyzer® (Beckman Coulter Ltd.). The mean particle sizes for three particle types coded as M, F and FF were 27.09 μm , 15.45 μm and 3.32 μm , respectively. Figure 1 shows SEM images of the SAOED powders. Table 1 shows the detailed size information of SAOED particles, and Figure 2 shows the particle size distribution.

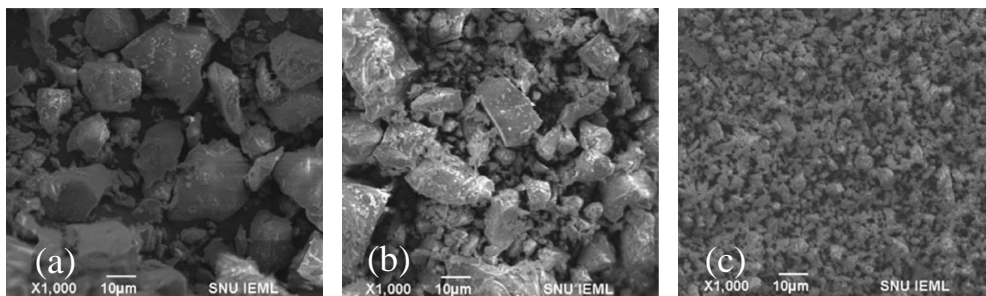


Figure 1. SEM images of SOAED powders. (a) M 27.09 μm (b) F 15.45 μm (c) FF 3.32 μm .

In our early study [90], the maximum intensity of green light from SAOED was shown at 520 nm wavelength by photoluminescence and mechanoluminescence (Figure 3). Characteristics of the stress-free persistence luminescence and mechanoluminescence are described in the literature [90-93].

Table 1. Particle size analysis results of SAOED powder.

	Mean dia. (μm)	Median dia. (μm)	S.D. (μm)	d_{90} (μm)
FF	3.328	3.131	2.158	6.381
F	15.46	12.44	12.42	33.91
M	27.09	26.28	17.60	51.27

Note: S.D. stands for standard deviation; d_{90} is the 90th percentile particle diameter.

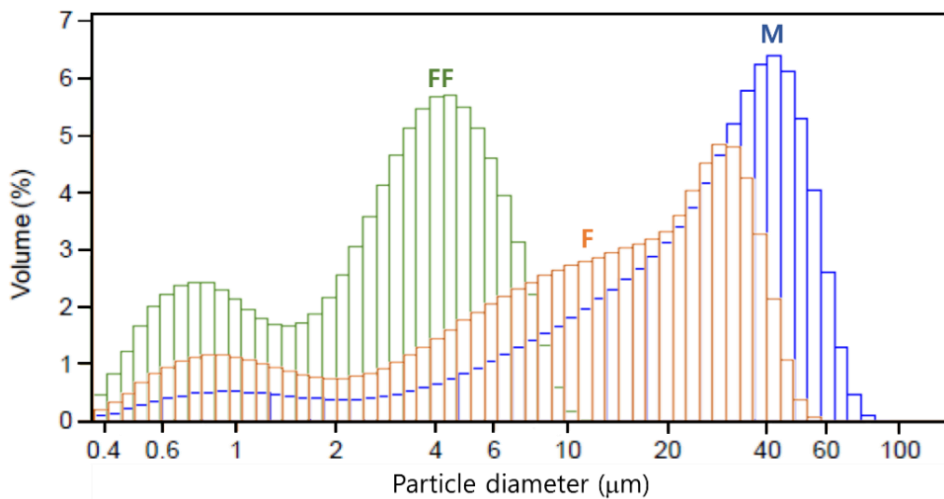


Figure 2. Particle size distribution of SAOED particles.

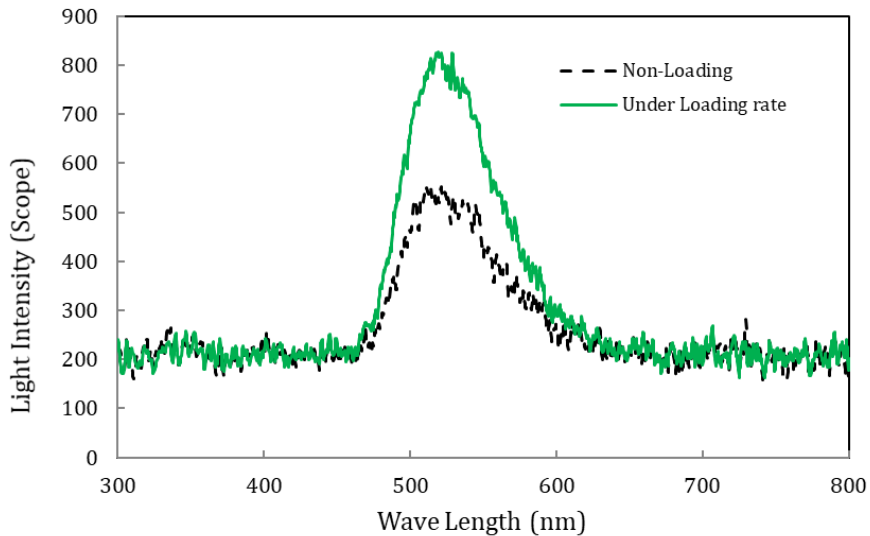


Figure 3. Mechanoluminescence of SAOED composites [90].

2.2. Ultrasonic curing treatment (UCT) manufacturing procedures

The silicone molds are made of Mold Max 30™ (Smooth-On, Inc). The molds were bonded on the up side of the metal sheet and the ultrasonic transducers were bonded on the down side. The ultrasonic transducers and ultrasonic generators were manufactured by Beijing Quanxin Ultrasonic Co. Ltd. 30 W ultrasonic transducers of three different frequencies, 40 kHz, 120 kHz and 200 kHz were employed in this study. The metal sheets are made of austenitic stainless steel; with its nonmagnetic property [91, 92], shields from electromagnetic interference that may affect the performance of the ultrasonic transducers. Photos of the UCT setup and detailed view of the metal sheets-transducer assembly are shown in Figure 4.

A weight ratio of 100 epoxy : 10 SAOED was simultaneously mixed and degassed using an impeller mixing machine inside a Lab1st® vacuum chamber

(~14.4 psi) for 5 min. Photos of the vacuum chamber and homemade mixer are shown in Figure 5.

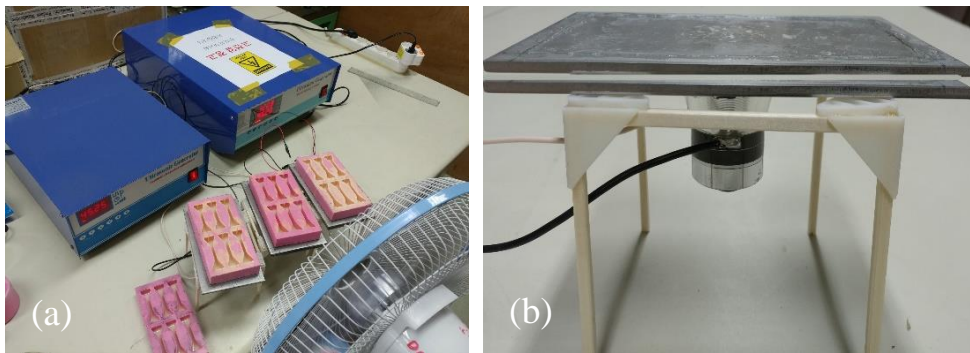


Figure 4. (a) UCT setup. (b) Metal sheets-transducer assembly.

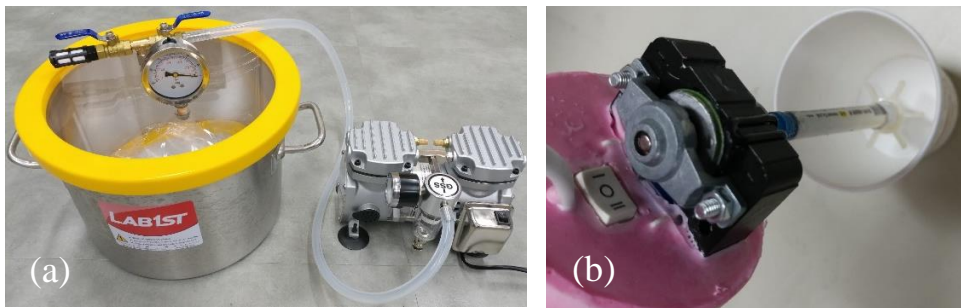


Figure 5. (a) Vacuum chamber and pump. (b) Impeller mixer for simultaneous degassing and mixing.

The degassed epoxy/SAOED composite in liquid state was poured into the dog-bone shaped molds and the ultrasonic generator turned on. Simultaneously a fan was turned on over the mold-sheet-transducer assemblies to avoid the creep. Both fan and ultrasonic generators were kept running for 7 hour nonstop. Finally, the ultrasonic generators were turned off after the 7 hour curing under sonication, then the hardened composite specimens were kept in room condition for another 4 days

to allow complete cure. A schematic overview of manufacturing process of epoxy/SAOED composite is illustrated in Figure 6.

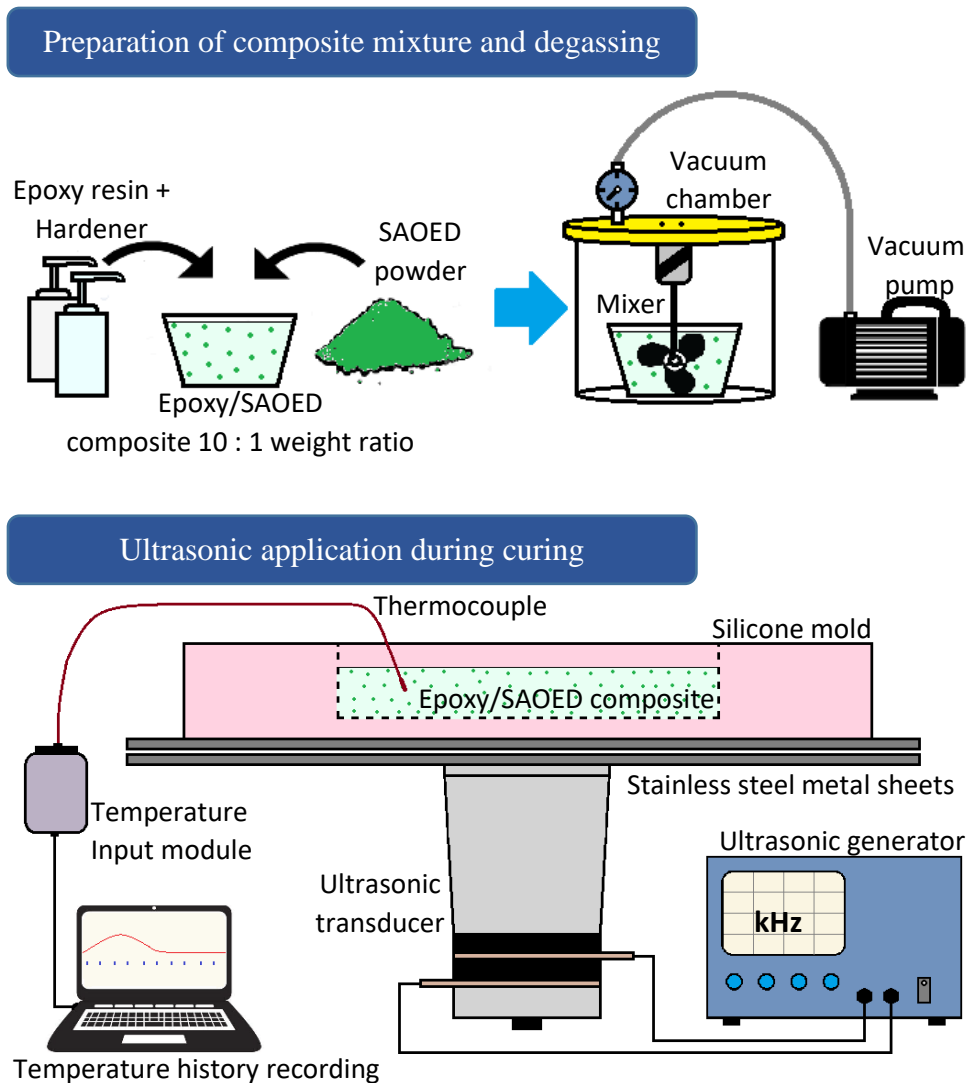


Figure 6. Schematic overview of epoxy/SAOED composite UCT manufacturing.

2.3. ML sensitivity test setup and procedure

Epoxy/SAOED composite dog-bone specimens with a thickness of 3 mm were manufactured from each frequency in order to compare their ML sensitivity. Specimen dimensions are shown in Figure 7. Manufacturing method is explained in Section 2.2.

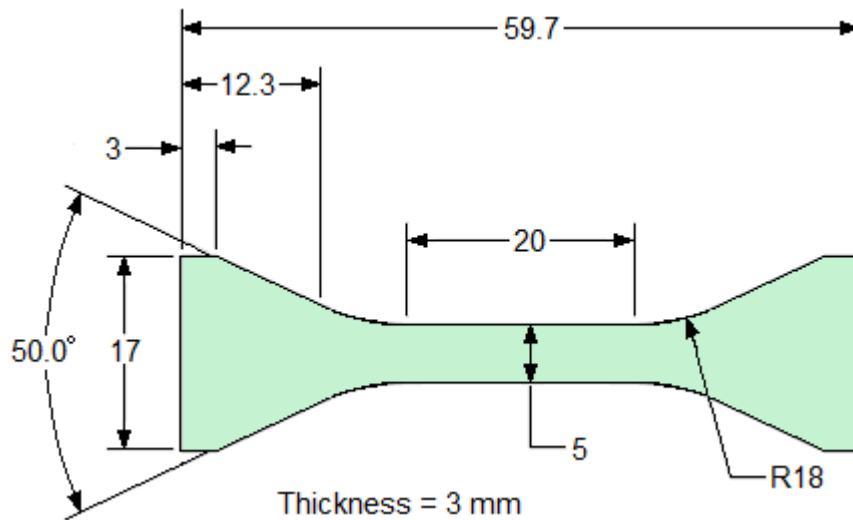


Figure 7. Dog-bone specimen dimensions.

The specimens were subjected to uniaxial tensile test and their ML reaction was video recorded. The images were evaluated using an image processing software applying a greyscale range for measuring the PIV (pixel intensity value), and the LI variation was analyzed for ML sensitivity analysis and minimum measurable strain analysis.

For ML sensitivity measurement, test procedures from previous literature [90, 93-95] were employed. Five specimens from each frequency, control 0 kHz; 40 kHz; 120 kHz and 200 kHz, were irradiated with 2100 cd light for 2 minutes. After that,

specimens were placed on the load frame in a complete dark environment and allowed to stress-free decay for 5 minutes. Next, the specimens were subjected to a maximum strain of 2.7% at 50 $\mu\text{m/s}$ speed using a μTS –Meso-Scale™ (Pylotech) load frame with wedge tension-type grips. A Grasshopper 3 4.1MP® (FLIR Systems, Inc.) camera was used in conjunction with PTGrey Fly Capture 2® (FLIR Systems, Inc.) software for video recording. Figure 8 shows photos of the ML sensitivity test setup and a detailed view of the load frame without the dark environment cover.



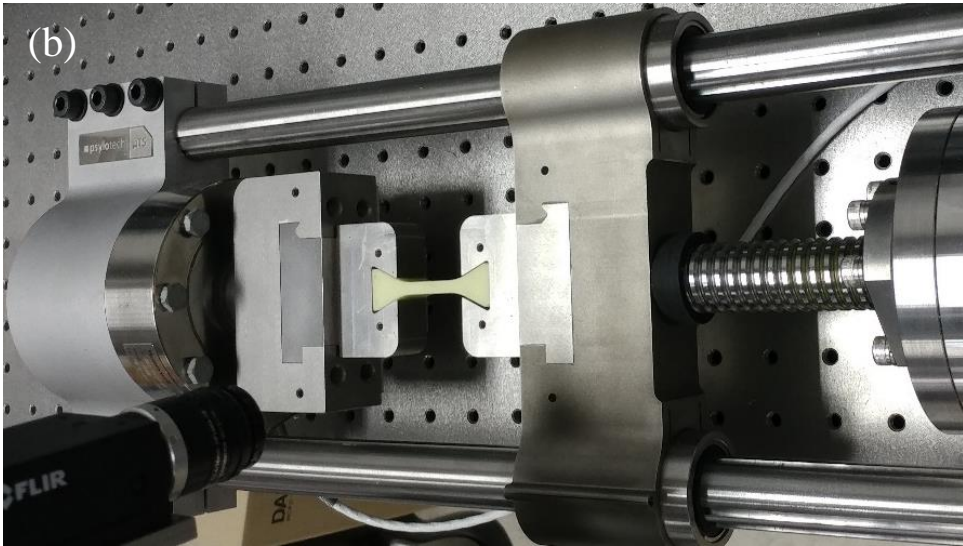


Figure 8. (a) Complete ML sensitivity test setup. (b) ML sensitivity test setup without dark environment cover.

The PIV was measured and the mean LI variation from the gauge area (100 mm^2) of the specimen was analyzed using the image processing software, FIJI ImageJ2® [96-98] as shown in Figure 9. A schematic drawing of the experimental setup is depicted in Figure 10.

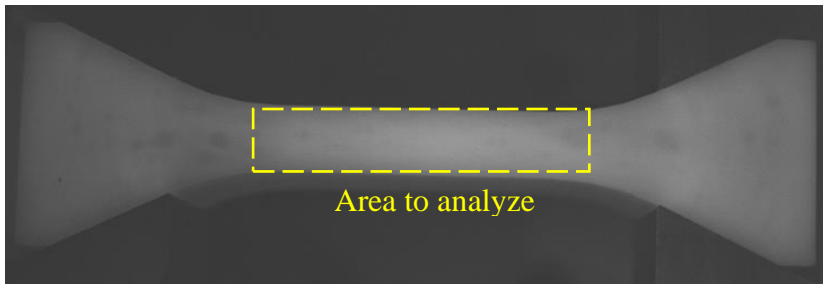


Figure 9. Image obtained during ML sensitivity test.

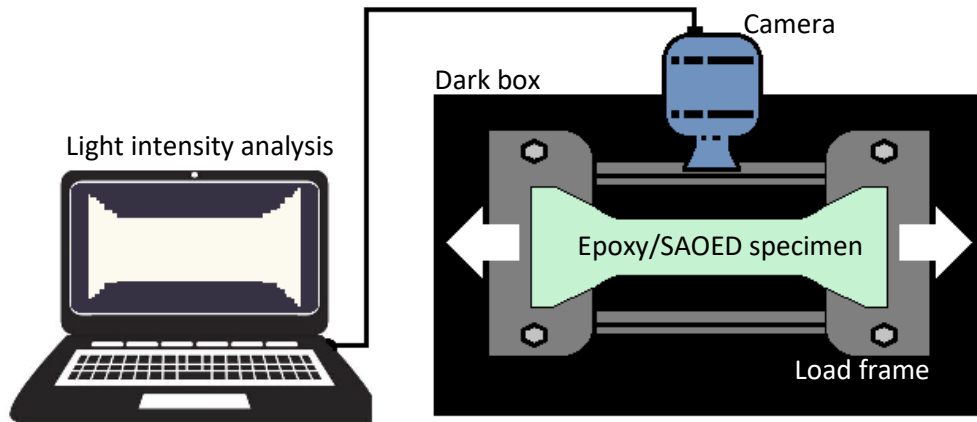


Figure 10. ML sensitivity test setup.

2.4. Minimum measurable strain test

The minimum measurable strain is an important factor for any ML material in order to be applied as a strain/stress sensor. From our tests, the ML sensitivity was significantly enhanced, and the minimum measurable strain was determined using the specimens treated with 120 kHz, which gave the highest ML sensitivity. In order to compare the ML sensitivity difference, control 0 kHz specimens were also subjected to this test. Tensile displacement was applied with a speed of 10 $\mu\text{m/s}$. A picture was taken every 5 μm of displacement increment. The three particle sizes, M, F and FF were examined in this experiment. The specimens were irradiated for 2 minutes, and allowed to stress-free decay until the gauge area reached a PIV of 100. After that, tensile strain was applied. The environmental setup for irradiation intensity, hardware and software setup for this test were the same as described in the ML sensitivity test. Results are presented in Section 3.2.

2.5 SEM analysis and micro-CT test

The surface morphology of the samples was observed using a field-emission scanning electron microscope (FE-SEM) J JSM-7800F Prime, Supra 55VP (JEOL Ltd.) with prior Pt sputter-coating at 30 mA for 30 sec using a Sputter Coater 108auto (Cressington Scientific Instruments Ltd.) The treatment resulted in about ~5 nm thickness of Pt coating.

A Skyscan 1275® (Bruker Corp.) scanner was used to perform micro-CT analysis in order to examine the particle dispersion in the composite. Image processing was conducted by an in-house MATLAB® code. Figure 11 represents the image processing flow where noise from the images was reduced applying Gaussian filter, Median filter and erosion. This improved the definition of interface between the particles. The Otsu's method was applied to define a proper threshold that discretizes the phase of particles and matrix. After binarization by Otsu's method, the image was divided using the watershed algorithm to distinguish the particles. In this research, size of the images is 300×600×933 (voxels) and its physical dimension is 5200 μm × 10400 μm × 17212 μm.

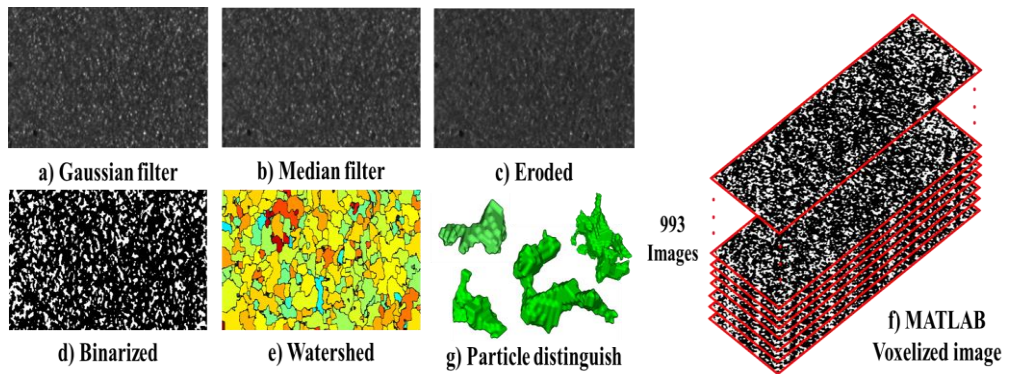


Figure 11. Image processing flow of raw image (a) → b) → c) → d) → e) → f) → g).

2.6 Temperature-monitoring during ultrasonic curing

During the UCT, heat might be generated by the sonicating action [99]. To minimize the effect of heat on interfacial bonding integrity between ML particles and epoxy resin, and to avoid the already mentioned heat-creep phenomenon, a fan was operated during the sonication process. Also, the in-situ temperature of composite mixture during the ultrasonic curing was monitored to examine any abnormal temperature peaks during the process. Three specimens from each frequency setup were monitored, using the equipment of cDAQ 9171 Compact DAQ Chassis; NI-9213 C Series Temperature Input Module; J- Type 482 °C thermocouples and DAQExpress (National Instruments Corp.) software for data visualization and recording. Sampling rate was 0.2 Hz (1 sample every 5 seconds). Recording went on for 5 hours and 12 minutes. Figure 12 shows the temperature-monitoring setup.

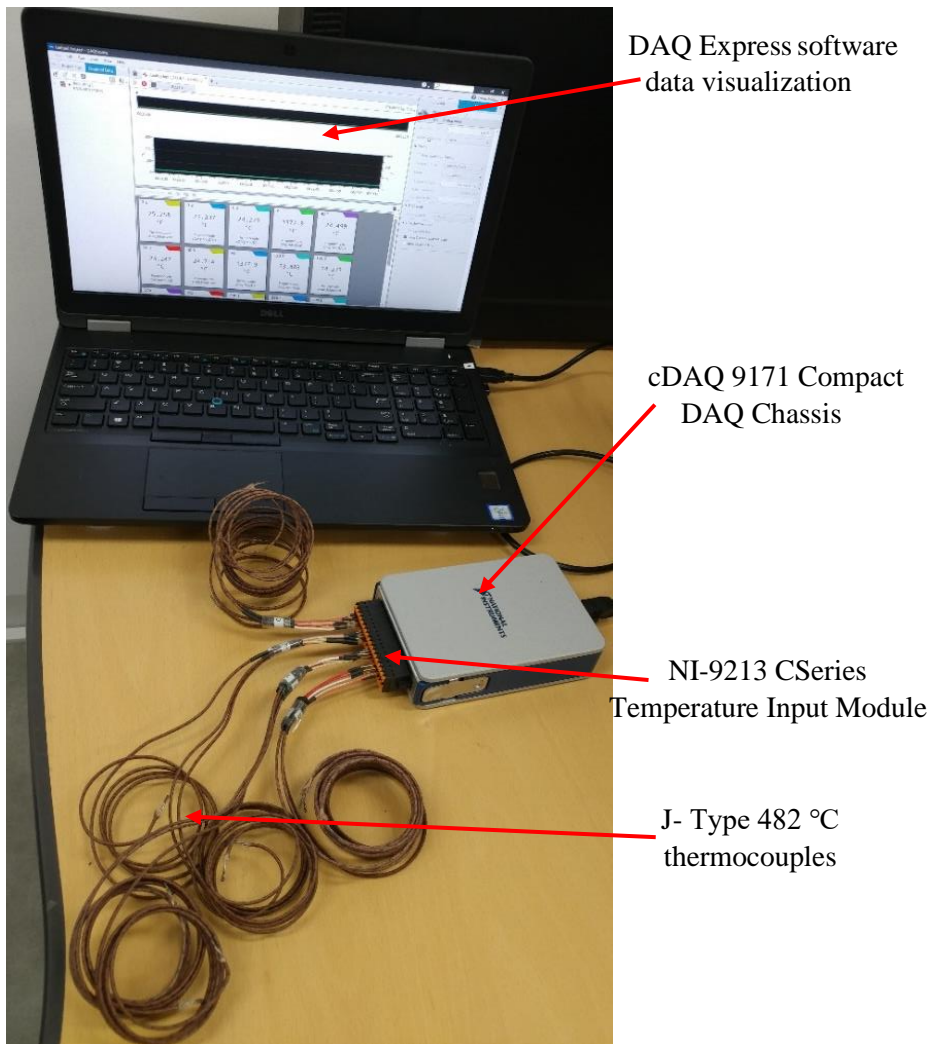


Figure 12. Temperature-monitoring setup.

As seen in Table 2, the results show there was no considerable temperature differences among the samples.

Table 2. Max temperature and time reached

Frequency	Thermocouple 1		Thermocouple 2		Thermocouple 3	
	Max Temp	Time	Max Temp.	Time	Max Temp	Time
0 kHz	34.3 °C	53' 15"	34.0°C	53' 10"	34.5 °C	52' 40"
40 kHz	33.9 °C	51' 00"	34.1 °C	50' 15"	34.6 °C	50' 45"
120 kHz	34.5 °C	48' 50"	34.2 °C	49' 30"	34.3 °C	48' 05"
200 kHz	34.0 °C	47' 25"	34.3 °C	47' 30"	35.1 °C	46' 40"

Figure 13 shows the complete temperature history graph of the 12 thermocouples. The temperature profiles and max temperatures obtained were the same in the four UCT samples and as expected for any standard epoxy resin curing reaction.

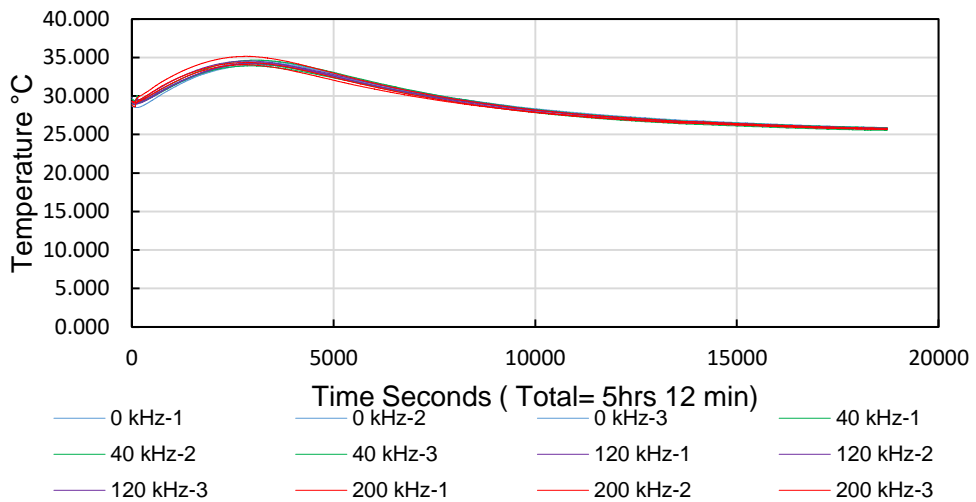


Figure 13. Temperature history profile graph of the 4 curing samples (3 thermocouples per sample).

3. Results and Discussions

3.1 ML sensitivity analysis

The results showed that the ML sensitivity was clearly increased by applying ultrasonic vibration during the hardening stage and the sensitivity increments are dependent on the sonication frequencies. However, the PL property remained unaltered. The four samples showed the same LI values after specimens were allowed to stress-free decay for 7 minutes. The graphs in Figure 14, Figure 15 and Figure 16 show the average LICR curves of 5 specimens from each group; 0 kHz control; 40 kHz; 120 kHz and 200 kHz. Each graph corresponds to a different SAOED particle size; M; F and FF.

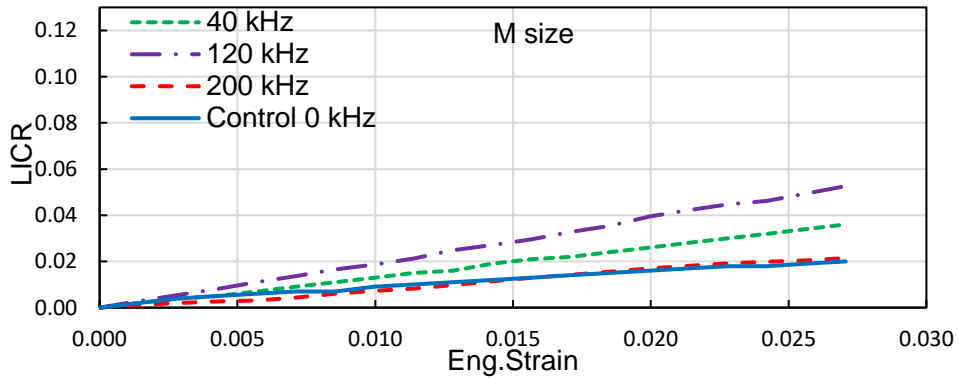


Figure 14. M size SAOED particles average LICR values.

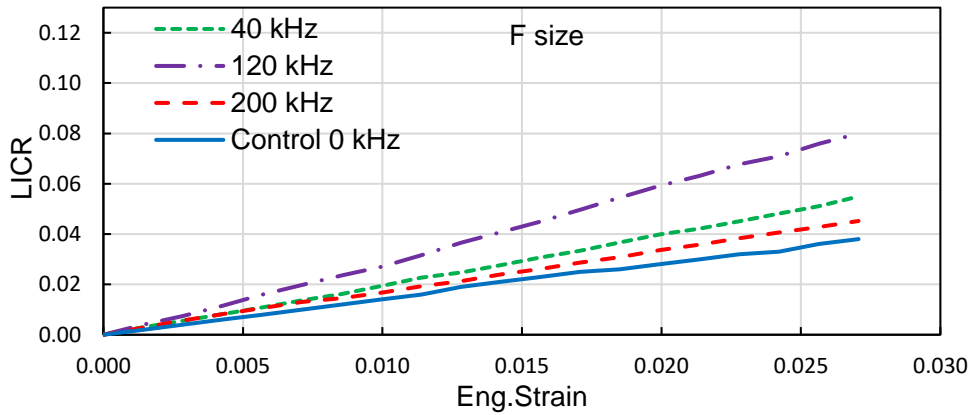


Figure 15. F size SAOED particles average LICR values.

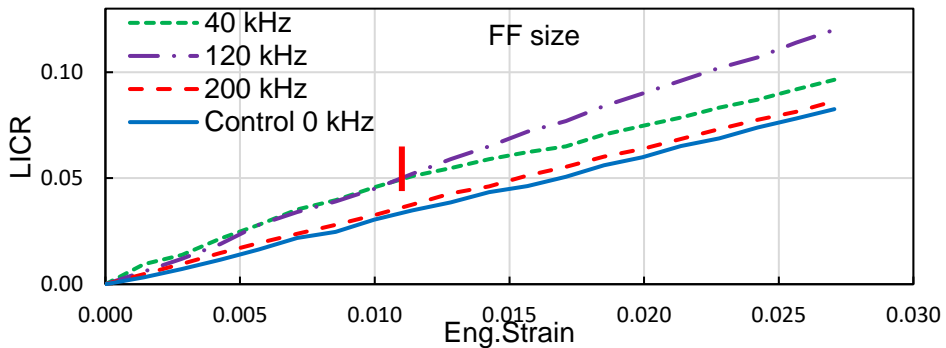


Figure 16. FF size SAOED particles average LICR values.

Table 3 shows the slope (i.e., sensitivity) from the average values of the LICR vs engineering strain curves. A higher value means a steeper slope, i.e. a higher ML sensitivity. Calculation of the ML sensitivity corresponds to the LICR sections between strain 0.005 and 0.025 applying a formula $ML\ sensitivity = LICR / (0.025 - 0.005)$. The averaged ML sensitivities in Table 3 are also compared in the bar graph Figure 17.

Table 3. Comparison of ML sensitivity for different frequencies and sizes.

Frequency	M size	F size	FF size
120 kHz	1.9191	2.9931	4.3000
40 kHz	1.3500	2.0076	3.1947
200 kHz	0.8659	1.6129	3.0924
0 kHz	0.6500	1.4000	3.0848

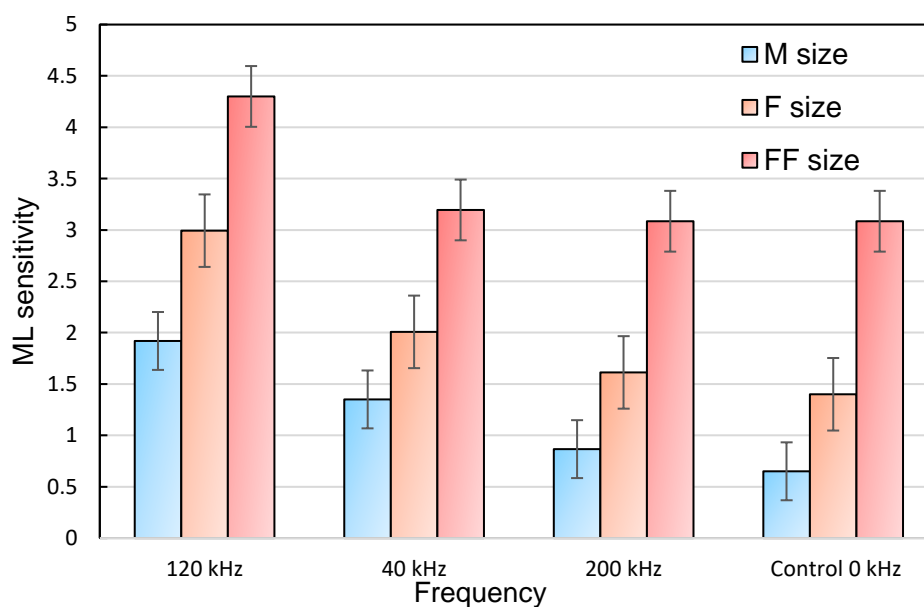


Figure 17. Comparisons of ML sensitivity for different sonication frequencies and sizes.

For this ML sensitivity analysis, we set ML sensitivity at 0 kHz as the reference (i.e., unit value). We will describe increase percentage of the ML sensitivity for different sonication frequencies. For the M particle size, the 120 kHz group showed 195% increment of ML sensitivity, which is the largest enhancement. The 40 kHz

and 200 kHz groups showed 108% and 33 % increases of the ML sensitivity, respectively. The 40 kHz group performs almost in the middle of 120 kHz and 200 kHz. The 120 kHz group has the highest ML sensitivity by a considerable difference.

For the F particle size, the 120 kHz group also has the highest ML sensitivity performance. The 120 kHz group showed 114% ML sensitivity increasing percentage referring the 0 kHz group. It is followed by the 40 kHz group that shows 43% increases of the ML sensitivity. However, 200 kHz group showed 15% increases of the ML sensitivity compared to 0 kHz group.

For the FF particle size, the 120 kHz group also showed the highest ML sensitivity. Compared to 0 kHz group, 120 kHz group showed 39% increases of the ML sensitivity. However, the 40 kHz and 200 kHz groups showed only 4% and 0.2% increases in the ML sensitivity through the section between 0.005 and 0.011 engineering strain. Interestingly, the 40 kHz group showed a bilinear strain-LICR response, kinking at 0.011 engineering strain. The 4 groups show the same ranking order regarding LICR performance for the 3 particle sizes. This demonstrates that the UCT methods successfully enhances the ML sensitivity property of the epoxy/SAOED composite. Moreover, the considerable difference of the 120 kHz happens with the 3 particle sizes. Furthermore, the similarity between the 0 kHz control and 200 kHz groups also repeats.

As reported in a recent literature [10], ML sensitivity of the FF size was distinctly the highest compared with other sizes. By setting ML sensitivity for M size to a reference (i.e., unit value), we also analyzed effects of ML sizes for each of the

sonication frequencies. For 0 kHz group, FF and F sizes showed 376% and 115% increases of the ML sensitivity, respectively. For 200 kHz group, FF and F sizes showed 257% and 86% increases, respectively. For 40 kHz group, FF and F sizes showed 137% and 49% increases, respectively. For 120 kHz group, FF and F sizes showed 124% and 56% increases, respectively. The particle size-dependence of ML sensitivity was reduced under UCT, as the overall ML sensitivity increased with application of UCT.

3.2 Minimum measurable strain analysis

The PL intensity decreases constantly while the specimen is subjected to tensile displacement until a certain strain is reached. For this reason, we considered that the minimal strain ML reaction occurs at the first indication of LICR downward trend counteract. As shown in Table 4, the 120 kHz specimens; the M particle specimen showed a minimal strain ML reaction of 9.972×10^{-4} ; the F particle specimen showed a minimal strain ML reaction of 8.547×10^{-4} and the FF particle specimen showed a minimal strain ML reaction of 7.123×10^{-4} . For the control 0 kHz specimens, the M particle specimen showed a minimal strain ML reaction of 1.2821×10^{-3} ; the F and FF particle specimens showed a minimal strain ML reaction of 1.1396×10^{-3} . The specimens subjected to the 120 kHz frequency UCT method require less strain in order to observe ML reaction, compared to the control 0kHz specimens. As expected, the sensitivity increases as SAOED particle size decreases. In other words, the smaller the particle the less strain is required to observe ML

reaction. However, the minimal strain ML sensitivity difference between the 3 particles sizes is relatively small. It's worth mentioning that even more specific values could be obtained if smaller tensile displacement increments are applied.

Table 4. Particle size and minimal strain ML reaction.

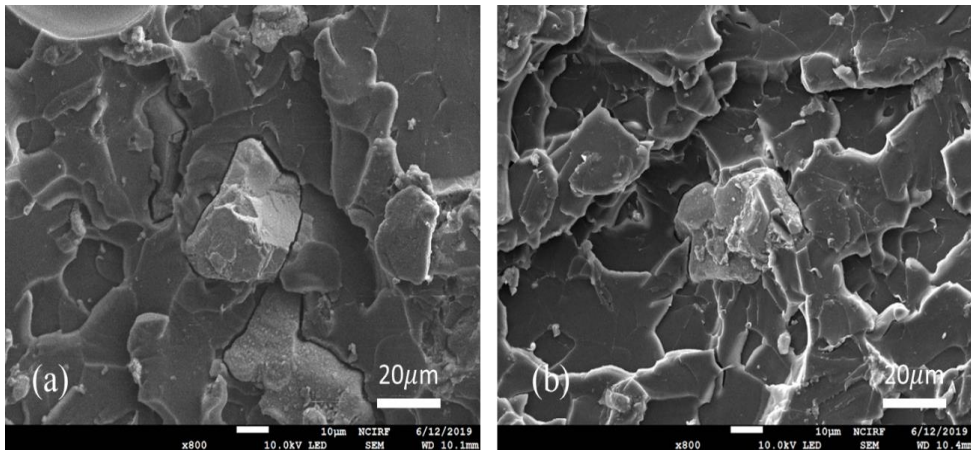
SAOED particle size	Minimum measurable 120 kHz	Minimum measurable 0 kHz
M	0.0009972	0.0012821
F	0.0008547	0.0011396
FF	0.0007123	0.0011396

3.3 Fractography for UCT Sonicated Interface Bonding with SEM.

3.3.1 Fractography after tensile test at room temperature

SEM images were taken from the fractured cross section area of specimens in order to observe the interfacial bonding and dislocation of the SAOED particles and epoxy resin. The fracture was induced during the uniaxial tensile test described in Section 2.3. Figure 18. shows the images from the 4 frequency specimen groups and M 27.09 μm particle size. Focusing on the interfacial bonding, interfacial bonding states observed in the images are consistent with the results obtained in the ML sensitivity analysis. Physically, higher ML sensitivity and low minimum measurable strain are attributed to effective stress transfer from epoxy resin to ML particles. Figure 18 (a) and (b) shows a weak interfacial bonding of 0 kHz group. A gap around the entire perimeter of the particles can be observed in 0 kHz group. Figure 18. (c) and (d) of a 40 kHz specimen show relatively well bonded perimeter around the

particle to the epoxy. However, small section of the perimeter presents gaps and there is an overall unevenness through the perimeter of the particle. In Figure 18(e) and (f) of a 120 kHz specimen, there is minimal gap or no gap all around the perimeter of the particles. Moreover, the particle at the center of the Figure 18 (e) remains completely bonded to the epoxy although it was severely fractured when pulled by tensile loading. In Figure 18 (g) and (h) of a 200 kHz specimen, although no gap can be seen through the perimeter of the particles, there are voids left from other particles where completely teared out from the epoxy. Furthermore, the surface of these voids is porous, possibly as a result of the micro-bubbles generated on the surface of the particles due to the strong agitation from the high ultrasonic frequency [87].



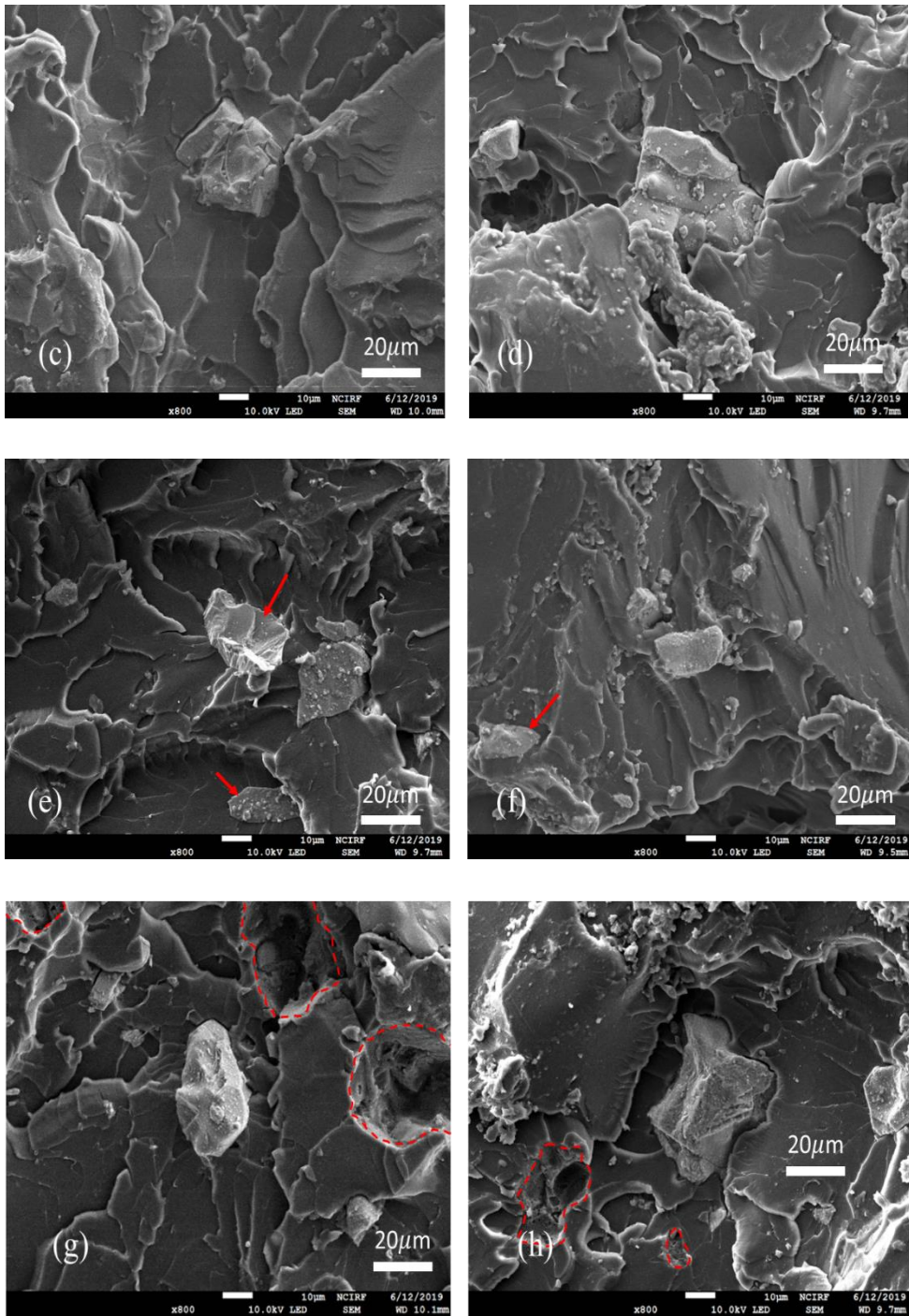
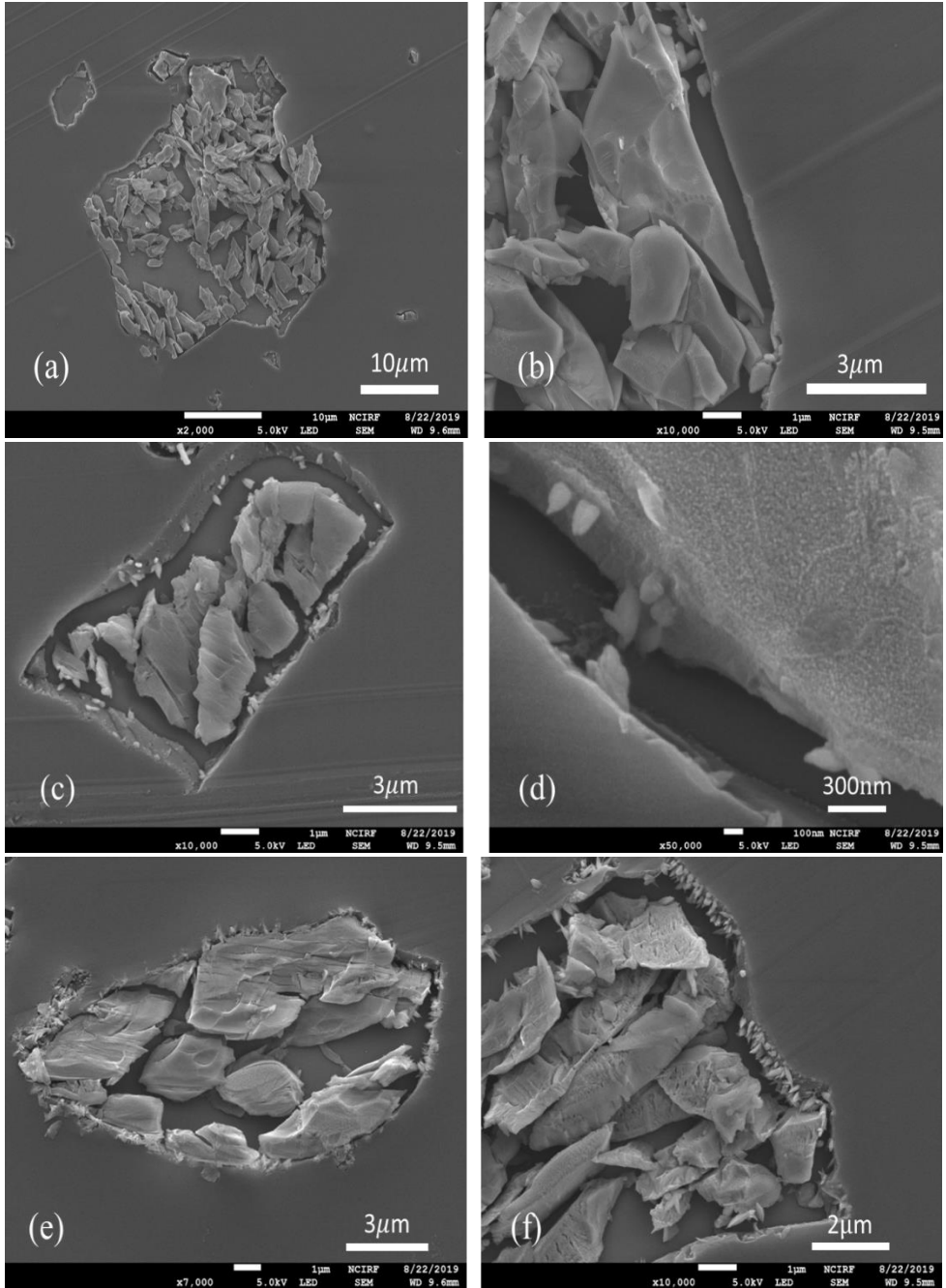


Figure 18. SEM of the fractured cross section of M 27.09 μm particle size (a, b) 0 kHz, (c, d) 40 kHz, (e, f) 120 kHz and (g, h) 200 kHz.

3.3.2 Fractography with slicing action

A second SEM analysis was performed to specimens machined using a Leica EM UC7[®] microtome in order to obtain a clean-cut surface. 500 nm thickness layer samples were obtained by strong mechanical cutting action of the microtome diamond knife. Because of brittleness of SAOED particles and extremely thin sliced cutting, the SAOED particles are shredded after the microtome process. Moreover, because of collection of slices in a small water reservoir immediately after cutting and high specific weight of SAOED particles, parts of shredded particles are lost. From SEM images, we can directly observe and compare interfacial bonding integrity for different UCT frequencies. According to SEM image analysis, interfacial bonding integrity states were consistent with the order of experimental ML sensitivity. Figure 19 (a) and (b) of a control 0 kHz specimen show shredded particles clearly detached from the epoxy. Figure 19 (c) and (d) of a 40 kHz specimen indicates small pieces of shredded SAOED particles attached in the detached interface. This indicates slightly improved integrity by UCT sonication. However, surprisingly as shown in Figure 19, many small pieces of the SAOED particles are observed on the detached interface and moreover, SAOED particles are still attached with the epoxy resin. This strong evidence from the SEM images is well consistent with the highest ML sensitivity of 120 kHz group that is attributed to the effective stress-transfer from the epoxy resin to the SAOED particle. However, SEM images of the 200 kHz specimen as shown in Figure 19 (g) and (h) show similar interface integrity states with 0 kHz group.



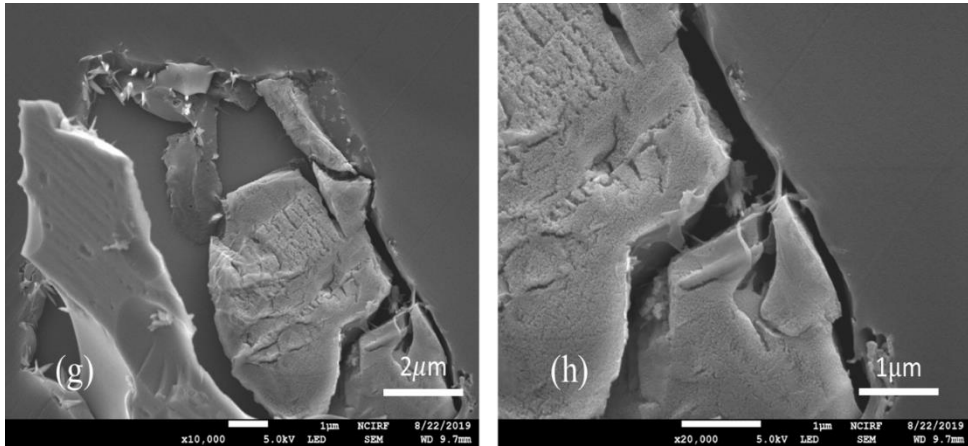


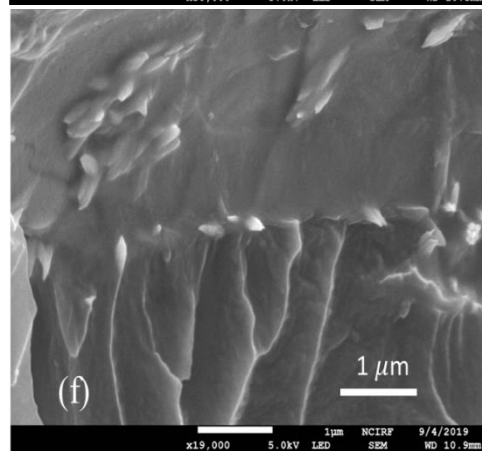
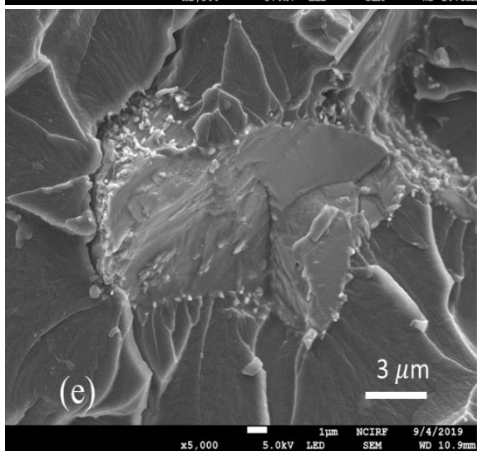
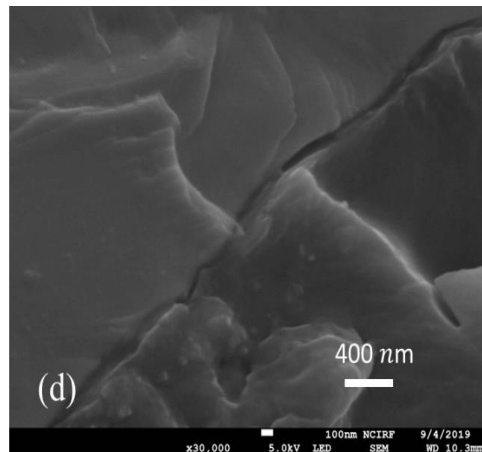
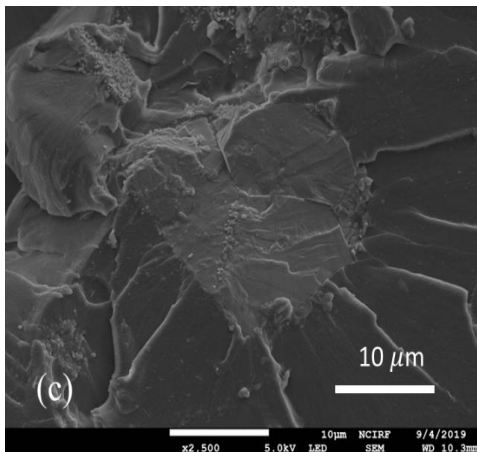
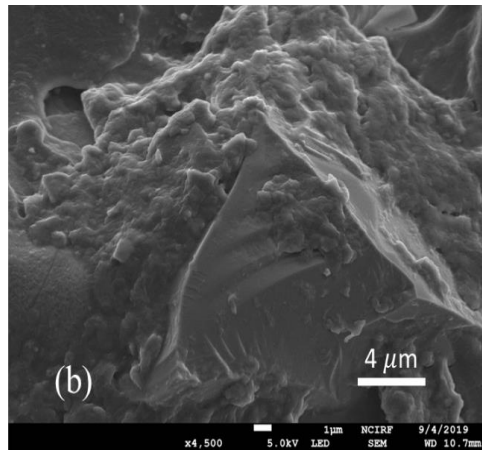
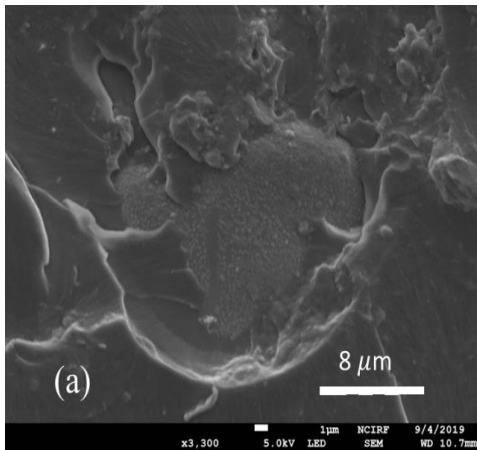
Figure 19. SEM of the microtome machined samples. F 15.45 μm particle size. (a), (b) 0 kHz. (c), (d) 40 kHz. (e), (f) 120 kHz. (g), (h) 200 kHz.

3.3.3 Fractography at cryogenic temperature

In order to observe bonded interface states between SAOED and epoxy, fractography analysis of cross sections fractured at cryogenic temperature is performed. Each specimen was submerged in liquid nitrogen for 90 seconds. The specimens were immediately fractured by hand once removed from the liquid nitrogen. In that way, it could be possible to observe in-tact interface. In this opportunity, energy-dispersive X-ray spectroscopy (EDS) was done simultaneously while observing the SEM images in order to evidence the particles. This was necessary due to the epoxy covering the particles.

Images from the fractured cross section area of the 4 frequency cryogenically are shown in Figure 21.

Figure 21 (a) and (b) of a control 0 kHz specimen show an exposed SAOED particle surface with epoxy resin attached around its perimeter. Epoxy resin appears to be detached from the SAOED surface. Un-fractured SAOED particle is another feature from the 0 kHz group, which means relatively low integrity of the interfacial bonding. Figure 21 (c) presents a clean cut through a SAOED particle in a 40 kHz specimen. From a closed-up of the interfacial part in Figure 21 (d), some gaps from slight interfacial debonding are observed through the partial perimeter of the particle. At least, this particle is cut through by the fracture action. As shown in Figure 21 (e) and (f) of the 120 kHz group, we could observe many small and sharp pieces mostly around the perimeter of the particle, which are certainly by the UCT sonication. The interface between SAOED and epoxy is clearly distinguished by the different fractured surface pattern. Well-bonded interface is also consistent with the highest ML sensitivity. Figure 20. 21 (g) and (h) from the 200 kHz specimen show a fractured cross section of a SAOED particle. Gaps between SAOED and epoxy by the interface debonding are also observed like the 0 kHz and 200 kHz group.



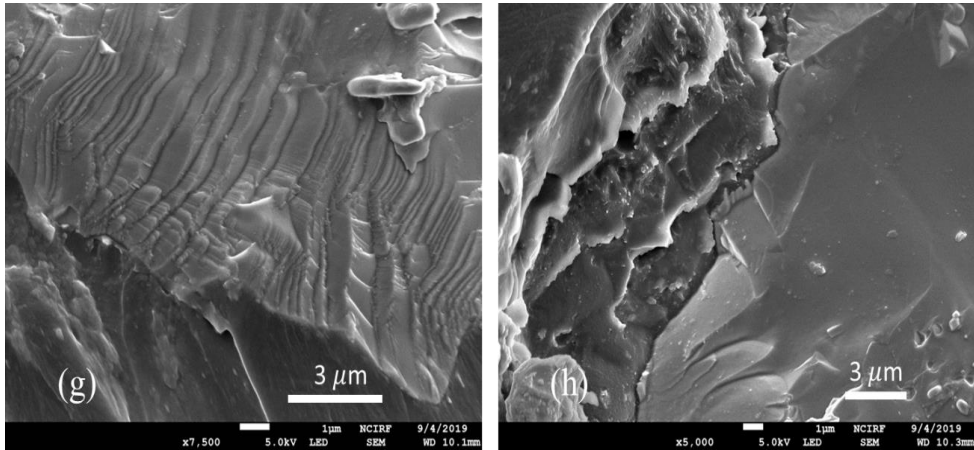


Figure 20. SEM of the cryogenically treated samples F 15.45 μm particle size. (a), (b) 0 kHz; (c), (d) 40 kHz; (e), (f) 120 kHz; (g), (h) 200 kHz.

3.4 Dispersions of UCT epoxy/SAOED Composites by Micro Computed Tomography

Micro-CT analysis was done to quantitatively compare the dispersion of composites according to the ultrasonic frequency. The morphological properties of the particles and their cumulative distributions were estimated in order to quantitatively compare the dispersion of composite.

3.4.1 Nearest Neighboring Distance

Nearest neighboring distance (NND) was defined as the minimum distance a particle geometrical centroid from another. The NND *i*-th value of the particle can be expressed as

$$NND^i = \min \left(\sum_{k=1}^3 \sqrt{(x_k^i - x_k^j)^2} \right) \text{ where } i \neq j \quad (1)$$

According to the definition of NND, every particle has one NND value and two particles that have the nearest distance shares the same NND value.

3.4.2 Quantitative Comparison According to the Ultrasonic Frequency

Figure 22 shows the specific views of the composites according to the 0 kHz; 40 kHz; 120 kHz and 200 kHz frequencies.

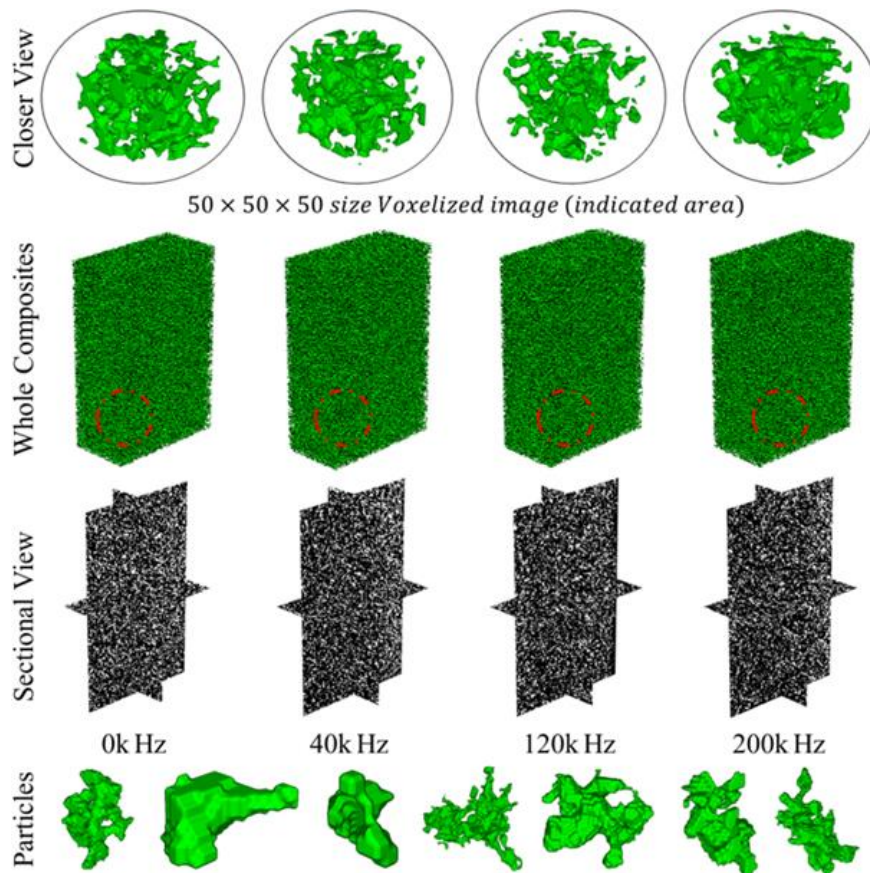


Figure 21. Schematics of the composites according to the ultrasonic frequency.

Voxel based models were obtained from the image processing flow, described previously. The volume, surface area, geometrical centroid and NND values of every particle were computed using the in-house MATLAB® code.

Table 5. Morphological Properties of the Particles in Composites.

Ultrasonic Wave Frequency	Number of Particles	Particle's Average Volume	Particle Average Surface Area	Particle Average NND
0 kHz	8663	5497.3	3504.3	16.7224
40 kHz	9790	4511.4	3028.8	15.3443
120 kHz	10756	4016.4	2678.5	14.7299
200 kHz	10202	4286.7	2884.3	15.0717

Table 5 shows the Morphological information of the particles in the composites of each frequency. The composite subjected to 120 kHz has the highest number of particles and the lowest average volume and surface area. This phenomenon suggests that for the 120 kHz, the particles has been broken by the ultrasonic pulse of the frequency and stress was efficiently applied to the particles. In addition, the 120 kHz frequency has the lowest average NND, indicating that the number of particles packed in a same volume was increased due to the influence of frequency pulse. This decrease of the average NND results in the increase particle number, i.e. particle density. We conclude that the increase of particle density also contributes to the ML sensitivity enhancement.

The cumulative distribution function of the NND of particles was examined to demonstrate the difference of NND and the dispersion of particles for each frequency. Figure 23 shows the NND of the particles in composite. The result shows that the cumulative probability increases for a same NND value varies from 0 kHz to 120 kHz and decreases from 120 kHz to 200 kHz. The higher cumulative probability value for same NND, the higher number of particle density, followed by 0 kHz, 40 kHz, 200 kHz, and 120 kHz. However, the number of particle density of the 40 kHz and 200 kHz was almost identical.

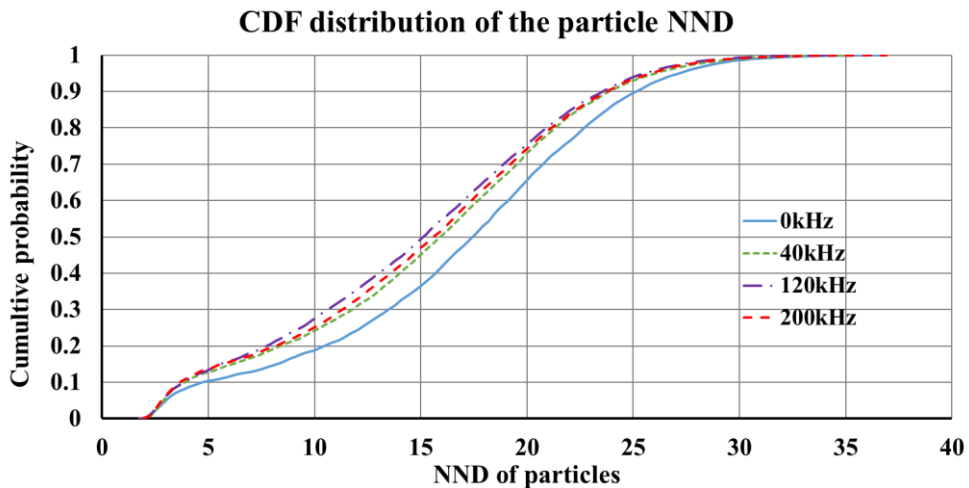


Figure 22. CDF distribution of the particle NND

The probability density function (PDF) of the particle surface area and volume was also evaluated to examine the effect on ML sensitivity of the composites, as depicted in Figure 24. The PDF of the surface area and volume for minimum to maximum value was evaluated and the PDF for small surface area and small volume was

examined to show the difference of the particle surface area and the volume for each frequency. Results show that the probability density in small volume range (20~200) increases in the order of 0 kHz; 200 kHz; 40 kHz and 120 kHz. This implies that the particles could be broken due to the ultrasonic pulse, as there are many particles in a small volume and surface area region. This result is identical to the ML sensitivity analysis in section 3.1. This suggests that ML sensitivity enhancement occurs as a result of the smaller volume of particles due to the breaking effect of the ultrasonic pulse.

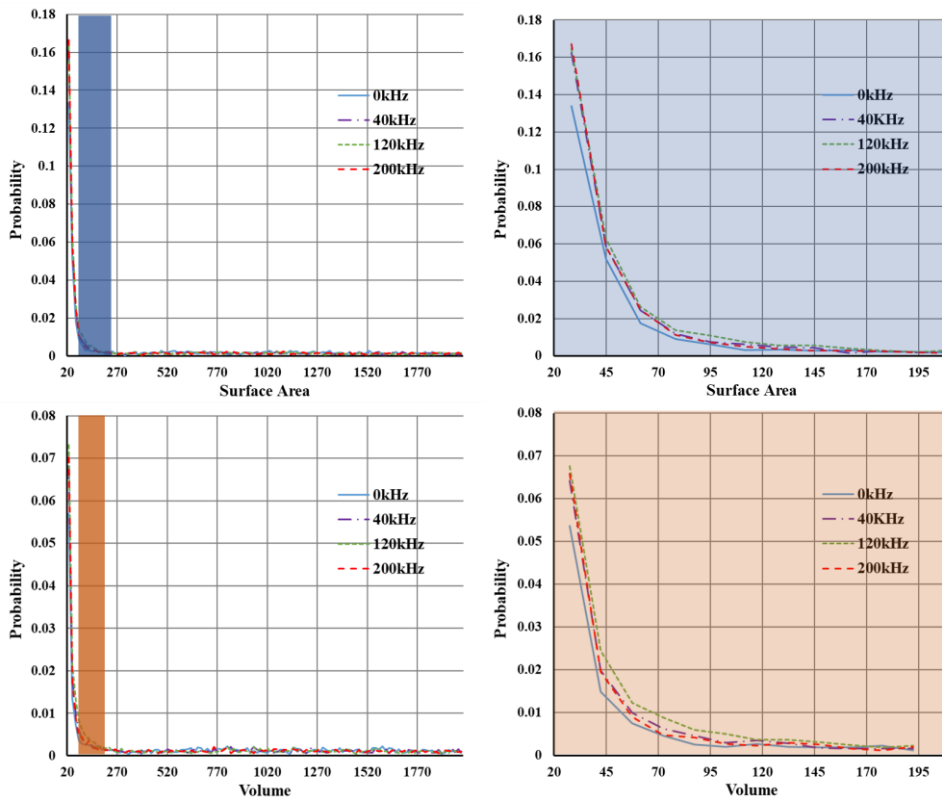


Figure 23. Probability Density Function of the Particle Surface Area and Volume.

3.5 Physical Mechanisms of Interfacial Bonding Augmentation by UCT

Method

Sonication of a liquid creates pressure waves in the liquid and microscopic bubbles from cavitation [100]. Cavitation effect is the sudden and explosive collapse of these bubbles that can generate “hot spots”, i.e. localized high temperature and high pressure shock waves, and severe shear force capable of breaking chemical bonds. Sonication enhance a variety of chemical and physical processes [99]. The nuclei of liquid subjected to ultrasonic frequency will expand or contract if the external pressure is made to change, and liquid will evaporate into the partial void produced. Although true voids are not present, this is the process generally referred to as cavitation, when the pressure changes are sufficiently large and rapid [101]. The higher surface release energy of the filler (particles or fibers) due to the cavitation resulting in good wetting of the fillers by the epoxy resin, which increases the molecular interaction at interface and in turn enhances the load transfer to the filler. Cavitation is likely to force epoxy resin into the interfibril or porous structure of the filler and increases the surface bonding, which contributes to increase the interlaminar shear strength (ILSS) [88]. Sonication decrease the viscosity and surface tension of the resin system, and increase the wettability due to the cavitation effect [87]. The group subjected to 120 kHz UCT method showed the highest LICR as a result of the relation between frequency and the size of cavitation nucleus cavitation [101]. For any assumed nuclear radius an upper threshold in frequency must exist above which the conditions for true cavitation can never be realized. An

increase in frequency for any given cavitation bubble size will result in the changes in bubble radius becoming less violent and finally degenerating into comparatively gentle oscillations as the frequency is increased above the resonant value of that particular size. Sometimes the change from cavitation to non-cavitation conditions will be a gradual one and no precise point can be fixed for the threshold. On the other hand, the change can be extremely sharp [102]. For a given cavitation nuclear size there is an optimal frequency that generates the most cavitation. On the other hand, the group subjected 200 kHz UCT method showed the lowest LICR because the effects of ultrasonic cavitation will cease above a certain frequency range as a consequence of the limitations in the expansion of the cavitation nucleus. Cavitation phenomena will diminish and finally disappear as the frequency is raised. [103]. When the ultrasonic frequency exceeded a certain value, the interfacial bonding decreased greatly. Under excessive treatment, ultrasonic etching action to the filler is so outrageous to produce a weak boundary layer on the fiber surface. This result in more micro-bubbles on the surface of the filler due to the stronger agitation action of ultrasound, which finally caused the weak point in the interlayer between the filler and matrix, and decreased the values of interfacial shear strength (IFSS) [87].

Due to the direct relation between the frequency propagation and the density of the media (epoxy) [104, 105], different results might be obtain if another brand of epoxy resin is used instead of the one used in this research.

4. Conclusion and Future Works

4.1 Conclusion

In this thesis, we present a novel approach to enhance the sensitivity of composite made with epoxy resin and strontium aluminate co-doped with europium ions and dysprosium ions by subjecting it to ultrasonic vibration throughout the hardening phase. Epoxy/SAOED composite in liquid state was poured into four separated molds in order to cast dog bone specimens. Three molds were subjected to a different ultrasonic frequency, 200 kHz, 120 kHz and 40 kHz for seven hours nonstop while the fourth mold was used as control sample with no frequency applied. This process was repeated three times using commercial SAOED powders with different average particle sizes, 27.09 μm , 15.45 μm and 3.32 μm . Once the curing time was completed, the specimens were subjected to tensile strain and their ML reaction was video recorded. The images were evaluated with an image processing software using greyscale values to measure the variation LI in order to generate a LICR analysis. SEM was used to observe the interphase bonding between particles and epoxy and micro-CT was implemented to perform dispersion analysis. The following conclusions can be drawn:

I. UCT method successfully enhances the ML property of epoxy/SAOED composite. All frequencies, 40 kHz, 120 kHz and 200 kHz generate an effect in the composite enhancing its ML property compared to the control 0 kHz specimens. The 120 kHz

frequency has the highest effect on the epoxy/SAOED composite while the 200 kHz has a minimal effect.

II. Epoxy/SAOED composite subjected to UCT method has ML property sensitivity increase. The 120 kHz specimens ML property reacts at less strain compared to the control 0 kHz specimens.

III. UCT has no effect on the PL property of epoxy/SAOED composite. The initial LI measurement is the almost identical in the 4 frequency groups. After 2 min irradiation and 5 min stress-free decay the M particle size has initial LI of 119.0 PIV for the 0 kHz and 118.7 PIV for the 120 kHz; F particle size has initial LI of 111.8 PIV for 0 kHz and 111.6 PIV for 120 kHz; FF particle size has initial LI of 101.9 PIV for 0 kHz and 102.0 PIV for 120 kHz. This was expected due to the fact that trapping system of SAOED PL is result from the piecemeal release of charge carriers from trapping centers and their successive combination at a luminescent center. Furthermore, the inherent characteristics of the particles size regarding PL and LICR prevail despite the UCT. In other words, the larger particle has better PL while the smallest particle has a better LICR. This behavior occurs as a result of different charge carrier traps levels from different particle sizes and the increase of dislocation density in SAOED decreases its stress-free afterglow while increasing its ML.

IV. ML sensitivity is enhanced in specimens subjected to UCT method due to the strengthening of the interfacial bonding. This was observed in the SEMs analyses. In addition, ML sensitivity is also enhanced by the particle density increase

generated by the breaking effect of the ultrasonic pulse. This was determined in the micro-CT dispersion analysis.

4.2. Future Works

The findings in this research contribute to the development of a super-sensitive ML stress/strain sensor composite capable to measure small strain values with high accuracy due to the enhanced sensitivity to elastic and plastic deformation. This novel technique can be applied to manufacture any kind of solid ML composite sensor. Further research should be carried out in order to develop an UCT method where the epoxy composite is subjected to different frequencies applied independently during specific periods throughout the curing process. Initially the epoxy is in liquid state, then enters into gelation state and finally into vitrification state; density of epoxy varies during the curing process and due to the relation between density of the media and frequency propagation, there is an ideal frequency for each density.

5. REFERENCES

1. Matsuzawa, T., et al., *A New Long Phosphorescent Phosphor with High Brightness, SrAl₂O₄: Eu²⁺, Dy³⁺*. Journal of the Electrochemical Society, 1996. **143**(8): p. 2670-2673.
2. Yamamoto, H. and T. Matsuzawa, *Mechanism of long phosphorescence of SrAl₂O₄: Eu²⁺, Dy³⁺ and CaAl₂O₄: Eu²⁺, Nd³⁺*. Journal of Luminescence, 1997. **72**: p. 287-289.
3. Clabau, F., et al., *Mechanism of phosphorescence appropriate for the long-lasting phosphors Eu²⁺-doped SrAl₂O₄ with codopants Dy³⁺ and B³⁺*. Chemistry of Materials, 2005. **17**(15): p. 3904-3912.
4. Liu, R.-S., *Phosphors, up conversion nano particles, quantum dots and their applications*. Vol. 1. 2016: Springer.
5. Jeong, S.M., et al., *Color manipulation of mechanoluminescence from stress-activated composite films*. Advanced Materials, 2013. **25**(43): p. 6194-6200.
6. Wang, X., et al., *Dynamic pressure mapping of personalized handwriting by a flexible sensor matrix based on the mechanoluminescence process*. Advanced Materials, 2015. **27**(14): p. 2324-2331.
7. Sohn, K.S., et al., *Direct observation of crack tip stress field using the mechanoluminescence of SrAl₂O₄:(Eu, Dy, Nd)*. Journal of the American Ceramic Society, 2002. **85**(3): p. 712-714.
8. Azad, A.I., M.R. Rahimi, and G.J. Yun, *Quantitative full-field strain measurements by SAOED (SrAl₂O₄: Eu²⁺, Dy³⁺) mechanoluminescent materials*. Smart Materials and Structures, 2016. **25**(9): p. 095032.
9. Li, C., et al., *Real-Time Visualisation of the Portevin–Le Chatelier Effect With Mechanoluminescent-Sensing Film*. Strain, 2011. **47**(6): p. 483-488.
10. Gnidakoung, J.R.N. and G.J. Yun, *Dislocation density level induced divergence between stress-free afterglow and mechanoluminescence in SrAl₂O₄: Eu²⁺, Dy³⁺*. Ceramics International, 2019. **45**(2): p. 1794-1802.
11. Xu, C.-N., et al., *Direct view of stress distribution in solid by mechanoluminescence*. Applied Physics Letters, 1999. **74**(17): p. 2414-2416.
12. Terasaki, N., et al., *Active crack indicator with mechanoluminescent sensing technique: detection of crack propagation on building 2012 IEEE Sensors Applications Symp.(SAS)*. 2012.
13. Timilsina, S., et al., *Optical evaluation of in situ crack propagation by using mechanoluminescence of SrAl₂O₄: Eu²⁺, Dy³⁺*. Journal of the American Ceramic Society, 2015. **98**(7): p. 2197-2204.

14. Sohn, K.-S., D.H. Park, and J.S. Kim, *Luminescence of pulsed-laser-deposited SrAl₂O₄: Eu, Dy thin film and its role as a stress indicator*. Journal of The Electrochemical Society, 2005. **152**(10): p. H161-H167.
15. Chandra, V. and B. Chandra, *Dynamics of the mechanoluminescence induced by elastic deformation of persistent luminescent crystals*. Journal of Luminescence, 2012. **132**(3): p. 858-869.
16. Chandra, B., V. Chandra, and P. Jha, *Microscopic theory of elasto-mechanoluminescent smart materials*. Applied Physics Letters, 2014. **104**(3): p. 031102.
17. Chandra, B., V. Chandra, and P. Jha, *Elastico-mechanoluminescence and crystal-structure relationships in persistent luminescent materials and II–VI semiconductor phosphors*. Physica B: Condensed Matter, 2015. **463**: p. 62-67.
18. Someya, S., et al., *Lifetime-based measurement of stress during cyclic elastic deformation using mechanoluminescence of SrAl₂O₄: Eu²⁺*. Optics express, 2014. **22**(18): p. 21991-21998.
19. Yun, G.J., et al., *Stress sensing performance using mechanoluminescence of SrAl₂O₄: Eu (SAOE) and SrAl₂O₄: Eu, Dy (SAOED) under mechanical loadings*. Smart Materials and Structures, 2013. **22**(5): p. 055006.
20. Kim, J.S. and G.-W. Kim, *New non-contacting torque sensor based on the mechanoluminescence of ZnS: Cu microparticles*. Sensors and Actuators A: Physical, 2014. **218**: p. 125-131.
21. Fu, X., H. Yamada, and C.-N. Xu, *Property of highly oriented SrAl₂O₄: Eu film on quartz glass substrates and its potential application in stress sensor*. Journal of the Electrochemical Society, 2009. **156**(9): p. J249-J252.
22. Brito, H.F., et al., *Persistent luminescence mechanisms: human imagination at work*. Optical materials express, 2012. **2**(4): p. 371-381.
23. Fujio, Y., et al., *Sheet sensor using SrAl₂O₄: Eu mechanoluminescent material for visualizing inner crack of high-pressure hydrogen vessel*. International Journal of Hydrogen Energy, 2016. **41**(2): p. 1333-1340.
24. Sohn, K.-S., et al., *A smart load-sensing system using standardized mechano-luminescence measurement*. Optics express, 2015. **23**(5): p. 6073-6082.
25. Zhang, J.-C., et al., *An intense elasto-mechanoluminescence material CaZnOS: Mn²⁺ for sensing and imaging multiple mechanical stresses*. Optics express, 2013. **21**(11): p. 12976-12986.
26. Terasaki, N., et al., *Hybrid material consisting of mechanoluminescent material and TiO₂ photocatalyst*. Thin Solid Films, 2009. **518**(2): p. 473-476.
27. Calderón-Olvera, R., et al., *Characterization of luminescent SrAl₂O₄ films doped with terbium and europium ions deposited by ultrasonic spray pyrolysis technique*. Ceramics International, 2018. **44**(7): p. 7917-7925.

28. Ono, D., et al., *Visualization of internal defect of a pipe using mechanoluminescent sensor*. Journal of the Japanese Society for Experimental Mechanics, 2010. **10**(Special_Issue): p. s152-s156.
29. Yamada, H., X.Y. Fu, and C.N. Xu. *Triboluminescence of SrAl₂O₄: Eu film with strong adhesion fabricated by a combination of RF magnetron sputtering and post-annealing treatment*. in *Key Engineering Materials*. 2008. Trans Tech Publ.
30. Fujio, Y., et al., *Development of highly sensitive mechanoluminescent sensor aiming at small strain measurement*. Journal of Advanced Dielectrics, 2014. **4**(02): p. 1450016.
31. Wang, W.X., et al. *A new smart damage sensor using mechanoluminescence material*. in *Materials Science Forum*. 2011. Trans Tech Publ.
32. Yun, G., et al., *Nondestructive Testing by Full-field Strains from Mechanoluminescent Sensors*. Materials Evaluation, 2016. **74**(6): p. 726-734.
33. Li, C., et al. *Real-time monitoring of dynamic stress concentration by mechanoluminescent sensing film*. in *Applied Mechanics and Materials*. 2008. Trans Tech Publ.
34. Jang, I.Y., et al. *Detection of reinforced concrete crack using mechanoluminescence paint*. in *Applied Mechanics and Materials*. 2013. Trans Tech Publ.
35. Kim, J.S., et al. *Detection of crack propagation in alumina using SrAl₂O₄:(Eu, Dy) luminescent paint*. in *Materials science forum*. 2007. Trans Tech Publ.
36. Kim, J.S., Y.-N. Kwon, and K.-S. Sohn, *Dynamic visualization of crack propagation and bridging stress using the mechano-luminescence of SrAl₂O₄:(Eu, Dy, Nd)*. Acta Materialia, 2003. **51**(20): p. 6437-6442.
37. Xu, J. and H. Jo, *Development of high-sensitivity and low-cost electroluminescent strain sensor for structural health monitoring*. IEEE Sensors Journal, 2016. **16**(7): p. 1962-1968.
38. Zhang, J.-C., et al., *Sacrificing trap density to achieve short-delay and high-contrast mechanoluminescence for stress imaging*. Acta Materialia, 2018. **152**: p. 148-154.
39. Li, J., et al., *Tailoring bandgap and trap distribution via Si or Ge substitution for Sn to improve mechanoluminescence in Sr₃Sn₂O₇: Sm³⁺ layered perovskite oxide*. Acta Materialia, 2018. **145**: p. 462-469.
40. Tu, D., et al., *Influence of H₃BO₃ addition on mechanoluminescence property of SrAl₂O₄: Eu²⁺*. Journal of the Ceramic Society of Japan, 2017. **125**(8): p. 648-651.
41. Zhan, T., et al. *Enhancement of impact-induced mechanoluminescence for structure health monitoring using swift heavy ion irradiation*. in *Behavior*

- and Mechanics of Multifunctional Materials and Composites 2012*. 2012. International Society for Optics and Photonics.
42. Clabau, F., et al., *On the phosphorescence mechanism in SrAl₂O₄: Eu²⁺ and its codoped derivatives*. Solid State Sciences, 2007. **9**(7): p. 608-612.
 43. Tang, M., et al., *Strong green and red up-conversion emission in Ho³⁺, Yb³⁺ and Li⁺ co- or tri-doped SrAl₂O₄ ceramics*. Journal of Alloys and Compounds, 2012. **529**: p. 49-51.
 44. Ryu, H. and K. Bartwal, *Defect structure and its relevance to photoluminescence in SrAl₂O₄: Eu²⁺, Nd³⁺*. Physica B: Condensed Matter, 2009. **404**(12-13): p. 1714-1718.
 45. Katsumata, T., et al., *Trap Levels in Eu-Doped SrAl₂O₄ Phosphor Crystals Co-Doped with Rare-Earth Elements*. Journal of the American Ceramic Society, 2006. **89**(3): p. 932-936.
 46. Diaz-Torres, L., et al., *Enhancing the white light emission of SrAl₂O₄: Ce³⁺ phosphors by codoping with Li⁺ ions*. Ceramics International, 2016. **42**(14): p. 16235-16241.
 47. Chen, L., et al., *A new green phosphor of SrAl₂O₄: Eu²⁺, Ce³⁺, Li⁺ for alternating current driven light-emitting diodes*. Materials Research Bulletin, 2012. **47**(12): p. 4071-4075.
 48. Qiang, R., et al., *Red emission in B³⁺- and Li⁺-doped SrAl₂O₄: Eu³⁺ phosphor under UV excitation*. Journal of Luminescence, 2009. **129**(8): p. 826-828.
 49. de Herval, L., et al., *Enhancement of the luminescence intensity by codoping Mn²⁺ into Er³⁺-doped SrAl₂O₄*. Journal of Luminescence, 2015. **163**: p. 17-20.
 50. Zhan, T., et al., *Enhancement of afterglow in SrAl₂O₄: Eu²⁺ long-lasting phosphor with swift heavy ion irradiation*. Rsc Advances, 2011. **2**(1): p. 328-332.
 51. Qiu, Z., et al., *Combustion synthesis of three-dimensional reticular-structured luminescence SrAl₂O₄: Eu, Dy nanocrystals*. Solid State Sciences, 2008. **10**(5): p. 629-633.
 52. Zhang, R., et al., *Gel combustion synthesis and luminescence properties of nanoparticles of monoclinic SrAl₂O₄: Eu²⁺, Dy³⁺*. Materials Chemistry and Physics, 2009. **113**(1): p. 255-259.
 53. Chen, J., F. Gu, and C. Li, *Influence of precalcination and boron-doping on the initial photoluminescent properties of SrAl₂O₄: Eu, Dy phosphors*. Crystal Growth and Design, 2008. **8**(9): p. 3175-3179.
 54. Yu, X., et al., *The influence of some processing conditions on luminescence of SrAl₂O₄: Eu²⁺ nanoparticles produced by combustion method*. Materials Letters, 2004. **58**(6): p. 1087-1091.

55. Lai, T.-T., et al., *Influence of Bi₂O₃ flux in the structural and photoluminescence properties of SrAl₂O₄: Eu²⁺ phosphors*. *Ceramics International*, 2013. **39**(1): p. 159-163.
56. Peng, T., et al., *Combustion synthesis and photoluminescence of SrAl₂O₄: Eu, Dy phosphor nanoparticles*. *Materials letters*, 2004. **58**(3-4): p. 352-356.
57. Rojas-Hernandez, R.E., et al., *Original synthetic route to obtain a SrAl₂O₄ phosphor by the molten salt method: Insights into the reaction mechanism and enhancement of the persistent luminescence*. *Inorganic chemistry*, 2015. **54**(20): p. 9896-9907.
58. Nakanishi, T., et al., *Enhanced Light Storage of SrAl₂O₄ Glass-Ceramics Controlled by Selective Europium Reduction*. *Journal of the American Ceramic Society*, 2015. **98**(2): p. 423-429.
59. Zhiping, X., et al., *Synthesis and luminescence properties of SrAl₂O₄: Eu²⁺, Dy³⁺ hollow microspheres via a solvothermal co-precipitation method*. *Journal of Rare Earths*, 2013. **31**(3): p. 241-246.
60. Ji, Z., et al., *Background illumination enhanced photo-stimulated up-conversion emission in persistent luminescent SrAl₂O₄:(Eu²⁺, Dy³⁺)*. *Ceramics International*, 2015. **41**(9): p. 11646-11650.
61. Ji, Z., et al., *Enhanced long lasting persistent luminescent SrAl₂O₄: Eu, Dy ceramics prepared by electron beam bombardment*. *Radiation Measurements*, 2013. **59**: p. 210-213.
62. Xu, Z., et al., *Wettability of carbon fibers modified by acrylic acid and interface properties of carbon fiber/epoxy*. *European polymer journal*, 2008. **44**(2): p. 494-503.
63. Luo, Y., et al., *Surface and wettability property analysis of CCF300 carbon fibers with different sizing or without sizing*. *Materials & Design*, 2011. **32**(2): p. 941-946.
64. Chen, P., et al., *Influence of fiber wettability on the interfacial adhesion of continuous fiber-reinforced PPESK composite*. *Journal of applied polymer science*, 2006. **102**(3): p. 2544-2551.
65. Greszczuk, L., *Theoretical studies of the mechanics of the fiber-matrix interface in composites*, in *Interfaces in composites*. 1969, ASTM International.
66. Drzal, L.T., et al., *Adhesion of graphite fibers to epoxy matrices: II. The effect of fiber finish*. *The Journal of Adhesion*, 1983. **16**(2): p. 133-152.
67. Drzal, L.T., M.J. Rich, and M.F. Koenig, *Adhesion of graphite fibers to epoxy matrices. III. The effect of hygrothermal exposure*. *The Journal of Adhesion*, 1985. **18**(1): p. 49-72.
68. Katzman, H.A., *Carbon-reinforced metal-matrix composites*. 1983, Google Patents.

69. Vilay, V., et al., *Effect of fiber surface treatment and fiber loading on the properties of bagasse fiber-reinforced unsaturated polyester composites*. Composites Science and Technology, 2008. **68**(3-4): p. 631-638.
70. Lee, W., J. Lee, and P. Reucroft, *XPS study of carbon fiber surfaces treated by thermal oxidation in a gas mixture of O₂/(O₂+ N₂)*. Applied Surface Science, 2001. **171**(1-2): p. 136-142.
71. Fukunaga, A., S. Ueda, and M. Nagumo, *Air-oxidation and anodization of pitch-based carbon fibers*. Carbon, 1999. **37**(7): p. 1081-1085.
72. Park, J., Y. Kim, and K. Kim, *Interfacial properties of ED carbon fiber reinforced epoxy composites using fragmentation techniques and acoustic emission*. Journal of Colloid Interface Science, 2000. **231**: p. 114-28.
73. Subramanian, R. and J.J. Jakubowski, *Electropolymerization on graphite fibers*. Polymer Engineering & Science, 1978. **18**(7): p. 590-600.
74. Yumitori, S. and Y. Nakanishi, *Effect of anodic oxidation of coal tar pitch-based carbon fibre on adhesion in epoxy matrix: Part 1. Comparison between H₂SO₄ and NaOH solutions*. Composites Part A: Applied Science and Manufacturing, 1996. **27**(11): p. 1051-1058.
75. Li, R., L. Ye, and Y.-W. Mai, *Application of plasma technologies in fibre-reinforced polymer composites: a review of recent developments*. Composites Part A: Applied Science and Manufacturing, 1997. **28**(1): p. 73-86.
76. Hamermesh, C. and P. Dynes, *The effect of plasma polymerization on the wettability of surfaces*. Journal of Polymer Science: Polymer Letters Edition, 1975. **13**(11): p. 663-668.
77. Brown, J. and Z. Mathys, *Plasma surface modification of advanced organic fibres: Part V Effects on the mechanical properties of aramid/phenolic composites*. Journal of materials science, 1997. **32**(10): p. 2599-2604.
78. Hwang, Y., et al., *Effects of atmospheric pressure helium/air plasma treatment on adhesion and mechanical properties of aramid fibers*. Journal of adhesion science and technology, 2003. **17**(6): p. 847-860.
79. Luo, S., et al., *Surface modification of textile tire cords by plasma polymerization for improvement of rubber adhesion*. Rubber chemistry and technology, 2000. **73**(1): p. 121-137.
80. Bell, J., et al., *Application of ductile polymeric coatings onto graphite fibers*. Polymer composites, 1987. **8**(1): p. 46-52.
81. Varelidis, P., R. McCullough, and C. Papaspyrides, *The effect on the mechanical properties of carbon/epoxy composites of polyamide coatings on the fibers*. Composites science and technology, 1999. **59**(12): p. 1813-1823.

82. Lin, T., et al., *The effect of chemical treatment on reinforcement/matrix interaction in Kevlar-fiber/bismaleimide composites*. Composites Science and Technology, 2000. **60**(9): p. 1873-1878.
83. Tarantili, P. and A. Andreopoulos, *Mechanical properties of epoxies reinforced with chloride-treated aramid fibers*. Journal of Applied Polymer Science, 1997. **65**(2): p. 267-276.
84. Day, R., K. Hewson, and P. Lovell, *Surface modification and its effect on the interfacial properties of model aramid-fibre/epoxy composites*. Composites science and technology, 2002. **62**(2): p. 153-166.
85. Drzal, L. and S. Ishihara. *Aramid fiber surface treatments to improve adhesion to epoxy matrices- Thermal and chemical treatments*. in *33 rd International SAMPE Technical Conference*. 2001.
86. Ma, H., et al. *Modification of carbon fiber and improvement of interfacial adhesion in epoxy resin composites with Co60 radiation*. in *Proceedings of 13th International Conference on Composites Materials, Beijing*. 2001.
87. Huang, Y., et al., *Influence of ultrasonic treatment on the characteristics of epoxy resin and the interfacial property of its carbon fiber composites*. Composites Science and Technology, 2002. **62**(16): p. 2153-2159.
88. Liu, L., et al., *Ultrasonic treatment of aramid fiber surface and its effect on the interface of aramid/epoxy composites*. Applied Surface Science, 2008. **254**(9): p. 2594-2599.
89. Liu, L., et al., *Effect of ultrasound on wettability between aramid fibers and epoxy resin*. Journal of applied polymer science, 2006. **99**(6): p. 3172-3177.
90. Yun, G.J., et al., *Stress sensing performance using mechanoluminescence of SrAl₂O₄:Eu (SAOE) and SrAl₂O₄:Eu, Dy (SAOED) under mechanical loadings*. Smart Materials and Structures, 2013. **22**(5).
91. Shyr, T.-W. and J.-W. Shie, *Electromagnetic shielding mechanisms using soft magnetic stainless steel fiber enabled polyester textiles*. Journal of Magnetism and Magnetic Materials, 2012. **324**(23): p. 4127-4132.
92. Wen, S. and D. Chung, *Electromagnetic interference shielding reaching 70 dB in steel fiber cement*. Cement and Concrete Research, 2004. **34**(2): p. 329-332.
93. Rahimi, M.R., et al., *Effects of persistent luminescence decay on mechanoluminescence phenomena of SrAl₂O₄:Eu²⁺, Dy³⁺ materials*. Optics Letters, 2013. **38**(20): p. 4134-4137.
94. Rahimi, M.R., G.J. Yun, and J.S. Choi, *A predictive mechanoluminescence transduction model for thin-film SrAl₂O₄:Eu²⁺, Dy³⁺ (SAOED) stress sensor*. Acta Materialia, 2014. **77**: p. 200-211.
95. Azad, A.I., M.R. Rahimi, and G.J. Yun, *Quantitative full-field strain measurements by SAOED (SrAl₂O₄:Eu²⁺, Dy³⁺) mechanoluminescent materials*. Smart Materials and Structures, 2016. **25**(9).

96. Rueden, C.T., et al., *ImageJ2: ImageJ for the next generation of scientific image data*. BMC bioinformatics, 2017. **18**(1): p. 529.
97. Schindelin, J., et al., *Fiji: an open-source platform for biological-image analysis*. Nature methods, 2012. **9**(7): p. 676.
98. Schneider, C.A., W.S. Rasband, and K.W. Eliceiri, *NIH Image to ImageJ: 25 years of image analysis*. Nature methods, 2012. **9**(7): p. 671.
99. Didenko, Y.T., W.B. McNamara, and K.S. Suslick, *Hot spot conditions during cavitation in water*. Journal of the American Chemical Society, 1999. **121**(24): p. 5817-5818.
100. West, R.D. and V.M. Malhotra, *Rupture of nanoparticle agglomerates and formulation of Al₂O₃-epoxy nanocomposites using ultrasonic cavitation approach: Effects on the structural and mechanical properties*. Polymer Engineering & Science, 2006. **46**(4): p. 426-430.
101. Noltingk, B.E. and E.A. Neppiras, *Cavitation produced by ultrasonics*. Proceedings of the Physical Society. Section B, 1950. **63**(9): p. 674.
102. Neppiras, E. and B. Noltingk, *Cavitation produced by ultrasonics: theoretical conditions for the onset of cavitation*. Proceedings of the Physical Society. Section B, 1951. **64**(12): p. 1032.
103. Gaertner, W., *Frequency dependence of ultrasonic cavitation*. The Journal of the Acoustical Society of America, 1954. **26**(6): p. 977-980.
104. Assia, O. and D. Hakim, *Propagation of ultrasonic waves in viscous fluids*, in *Wave Propagation in Materials for Modern Applications*. 2010, IntechOpen.
105. He, P. and J. Zheng, *Acoustic dispersion and attenuation measurement using both transmitted and reflected pulses*. Ultrasonics, 2001. **39**(1): p. 27-32.

국문초록
초음파 경화 법에 의한 $\text{SrAl}_2\text{O}_4 : \text{Eu}^{2+}, \text{Dy}^{3+}$
복합체의 기계 발광 감도

토마스 웨베 케레케스
기계항공공학부
서울대학교 대학원

이 논문은 에폭시 수지와 유로퓸 이온 및 디스프로슘 이온 (SAOED)과 함께 도핑 된 스트론튬 알루미늄 네이트로 제조 된 복합체의 기계적 발광 (ML) 감도를 경화 공정 전반에 걸쳐 초음파 진동에 노출시킴으로써 새로운 접근법을 제시한다. 에폭시 / SAOED 복합체의 4 가지 몰드에 상이한 초음파 주파수를 가 하였다; 200kHz; 120kHz; 40 kHz 및 제어 0 kHz. 경화 된 시편에 인장 변형을 가하고 그들의 ML 반응을 비디오 기록 하였다. ML 광도 변화율 (LICR) 분석 및 최소 측정 가능한 변형 ML 감도 평가를 생성하기 위한 광도 (LI) 변화를 얻기 위해 이미지를 분석 하였다. 주사 전자 현미경 (SEM)을 사용하여 각각의 샘플의 상간 결합 차이를 관찰하고, 마이크로-컴퓨터 단층 촬영 (micro-CT) 시험을 수행하여 복합체에서의 입자 분산을 검사 하였다. 결과는 경화 공정 동안 초음파 진동을 가하면 간 결합을 강화시켜 복합체의 ML 감도를 증가시키는 것으로 나타났습니다.

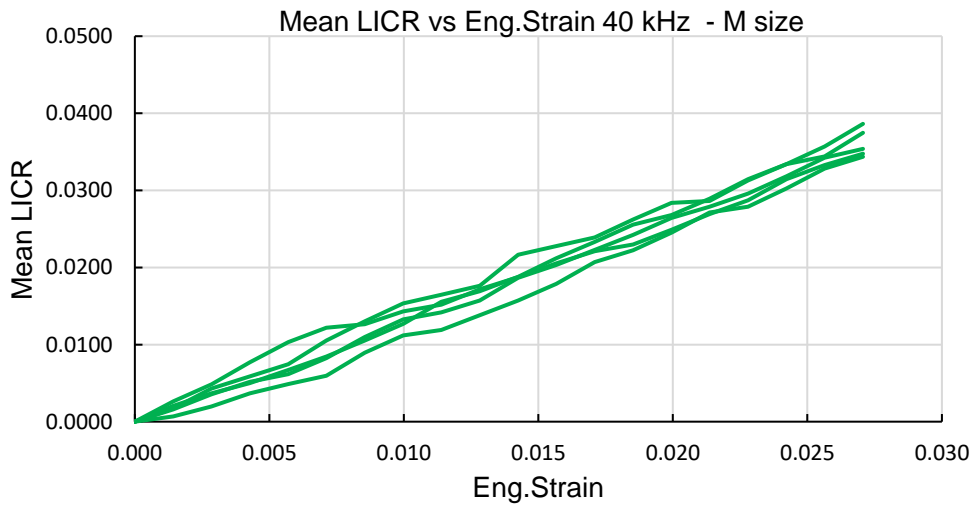
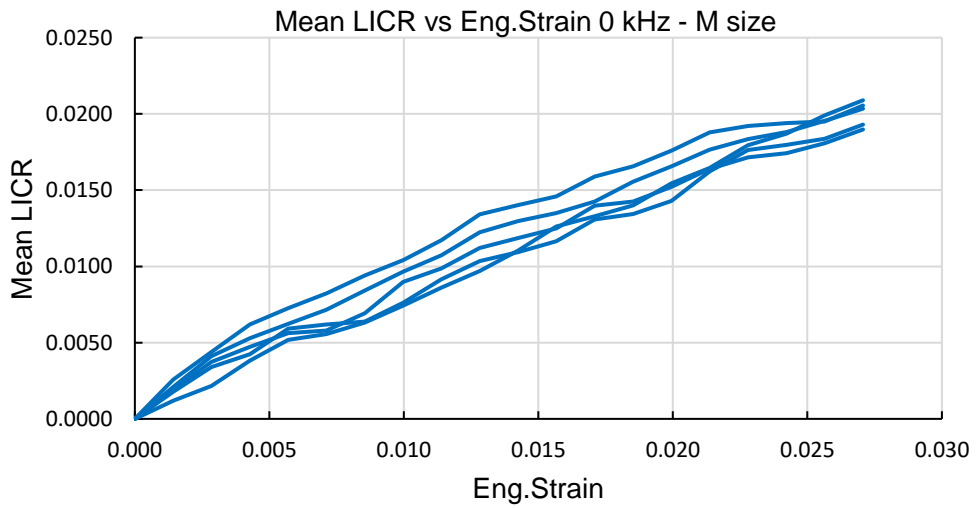
Keywords : 스트론튬 알루미늄 네이트, 기계적 발광, 초음파 진동, 습윤성, 응력
/ 변형 센서, 에폭시 / SAOED 복합재.

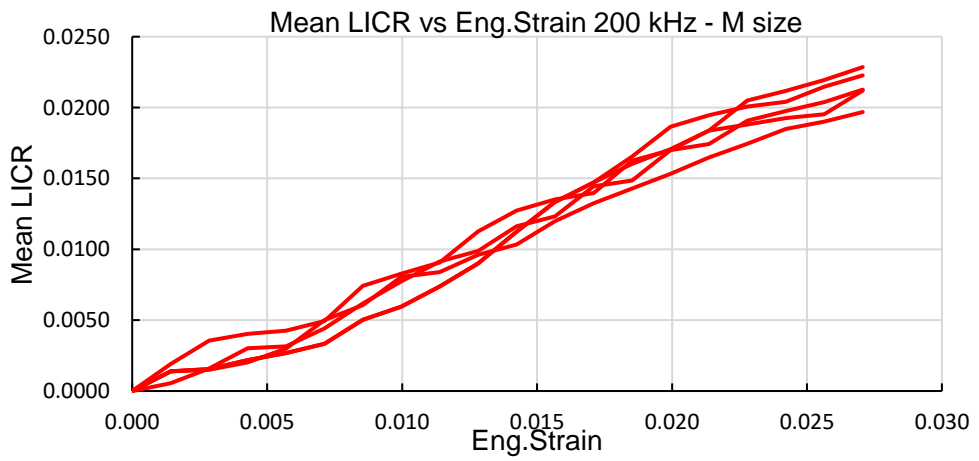
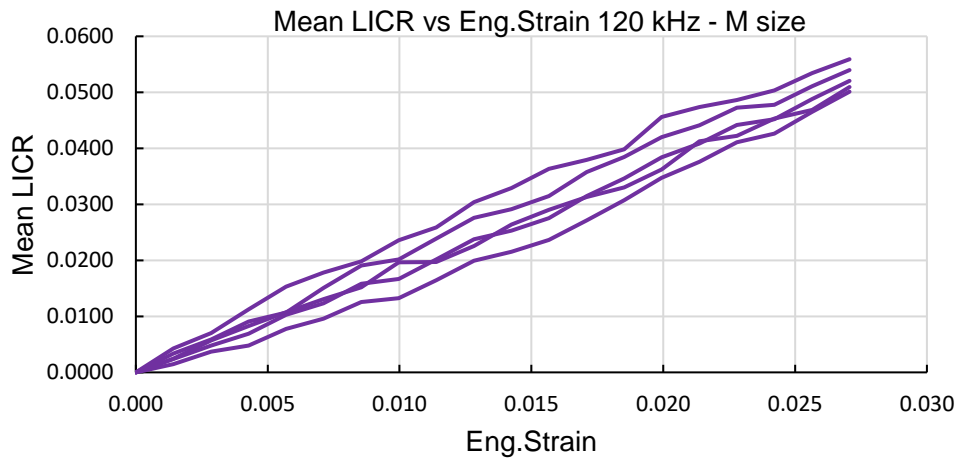
Student Number : 2017-24235

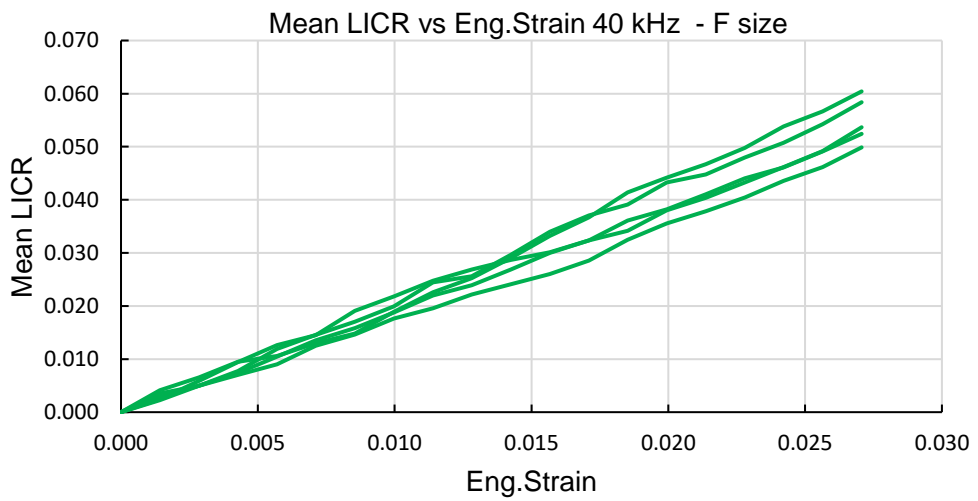
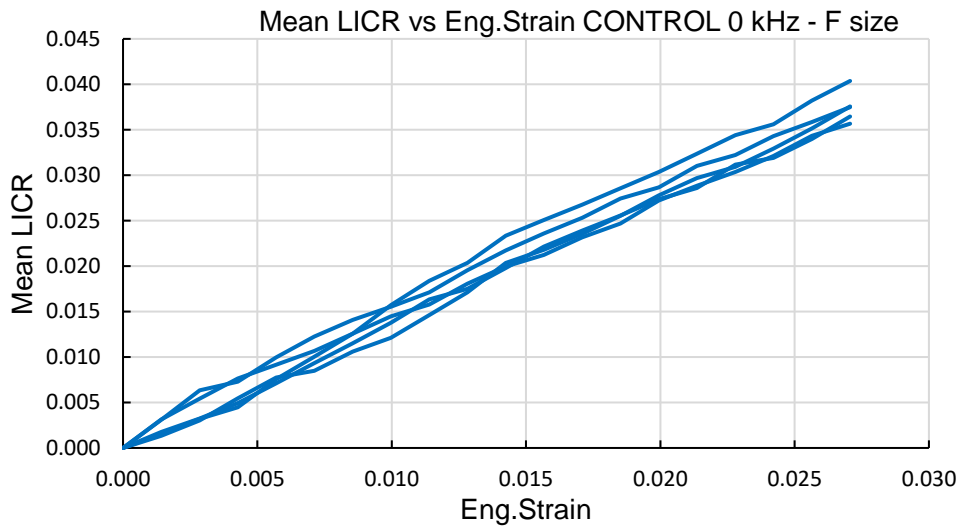
6. Appendices

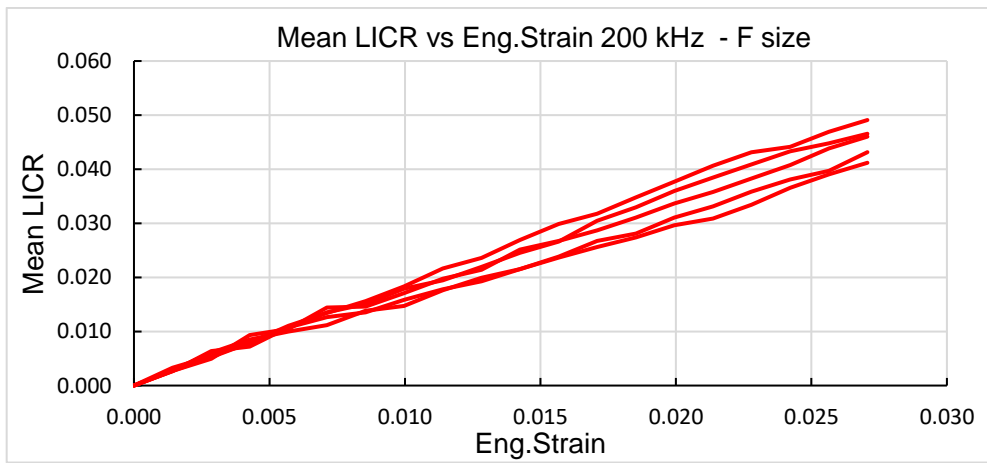
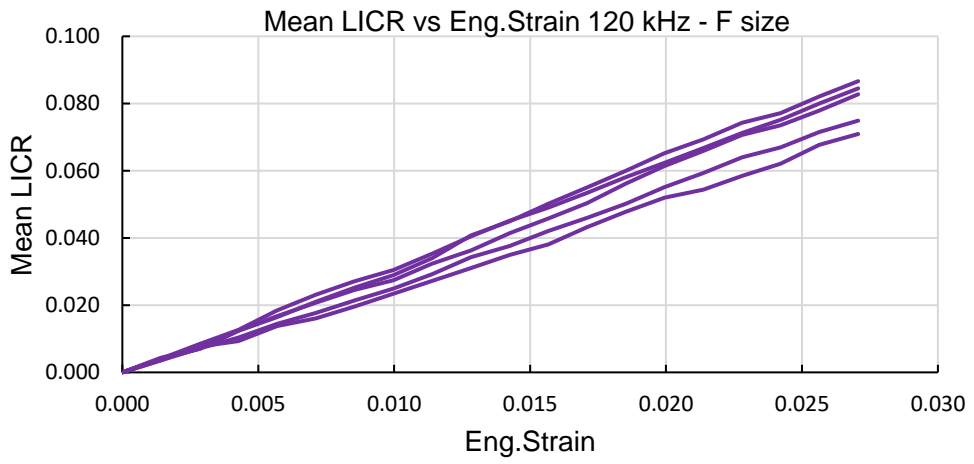
Appendix A. Experimental results

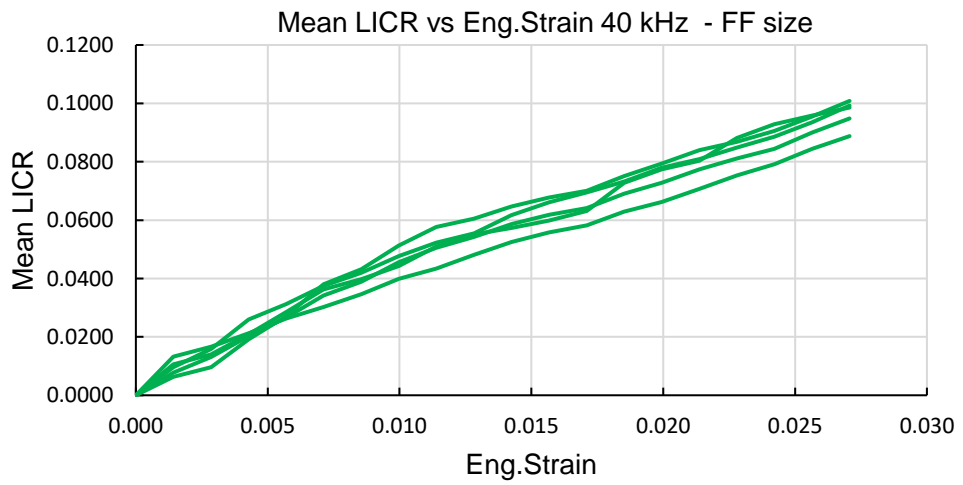
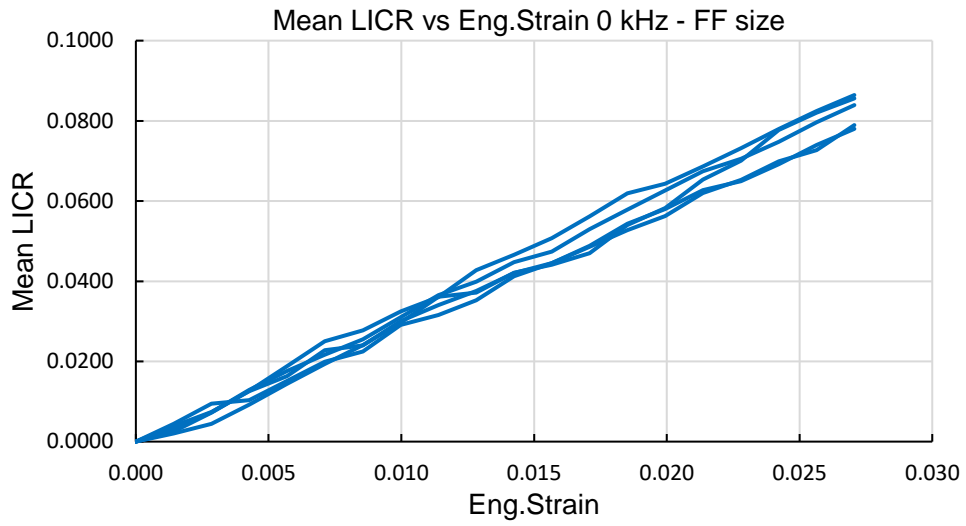
ML sensitivity results.

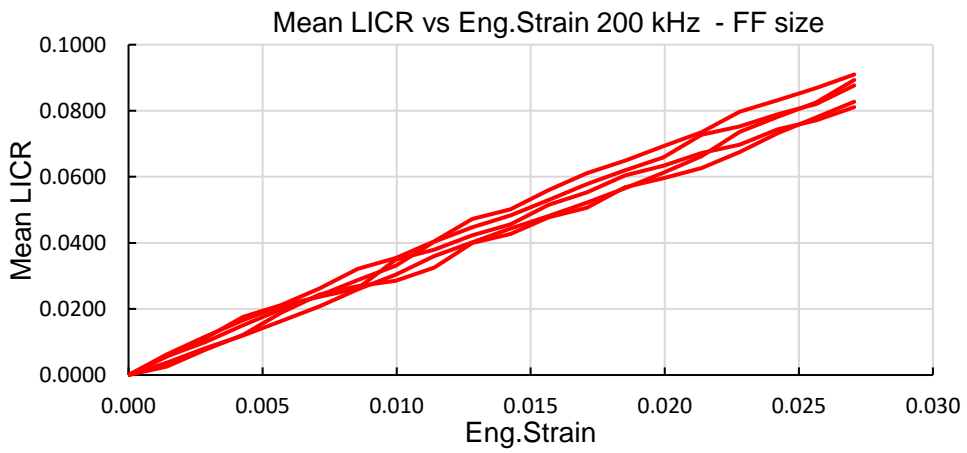
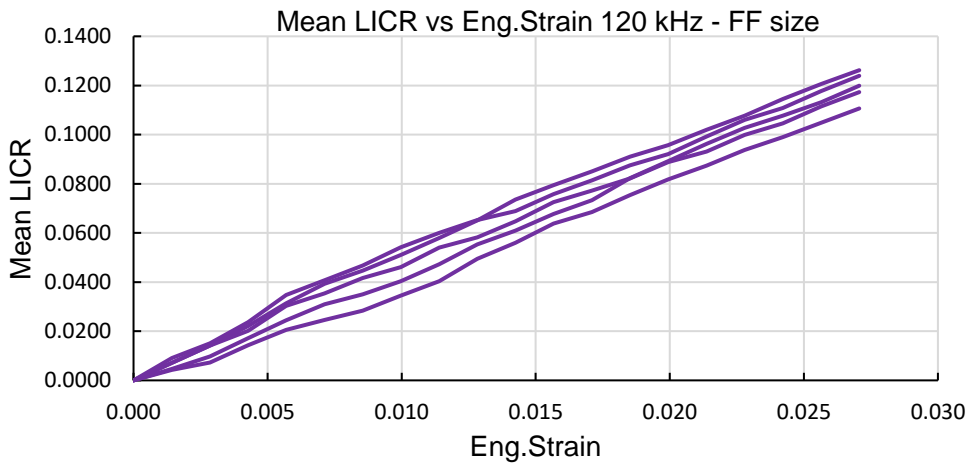




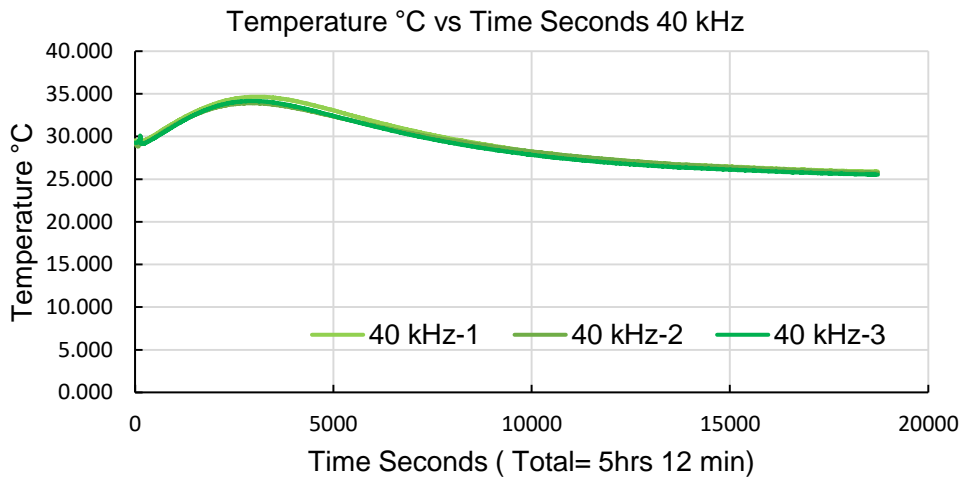
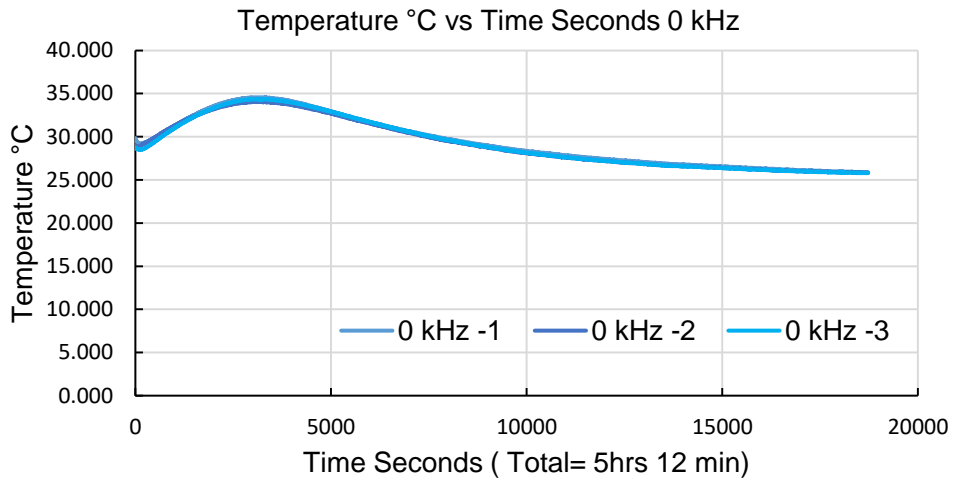


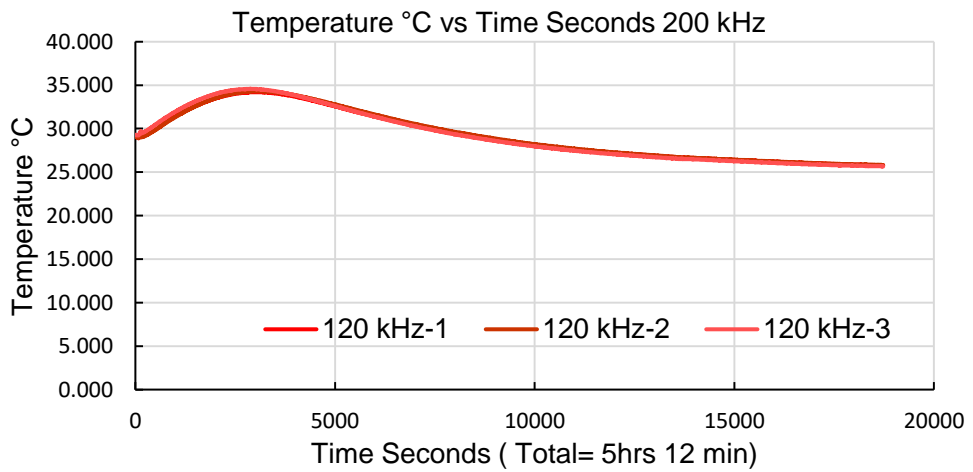
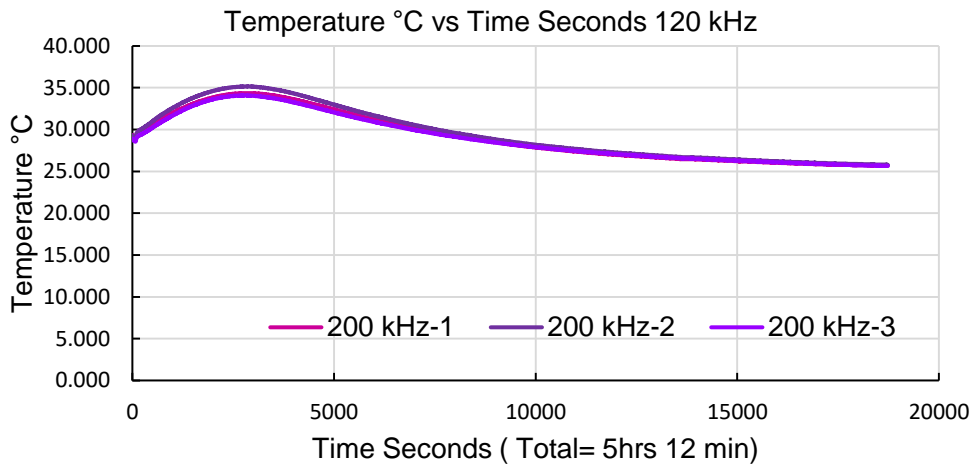






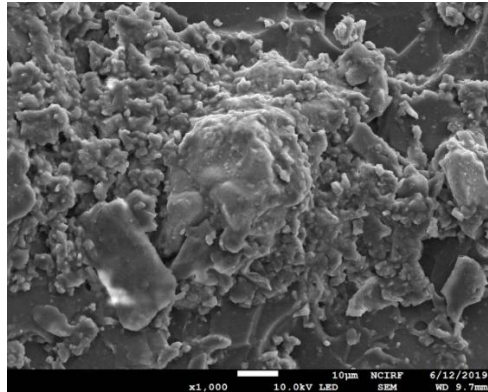
Temperature history results.



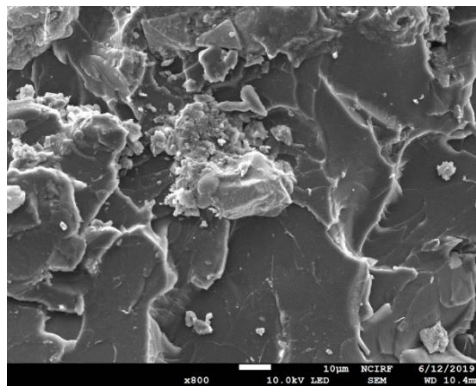


Appendix B. SEM images

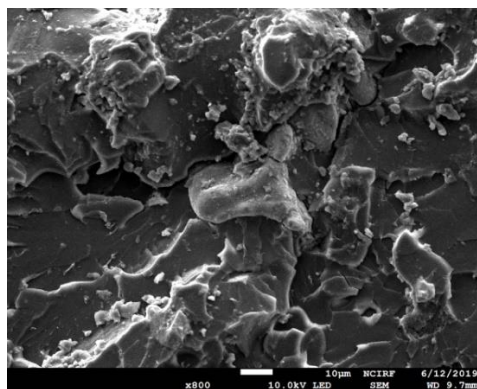
SEM images of fractured specimens at room temperature



0 kHz

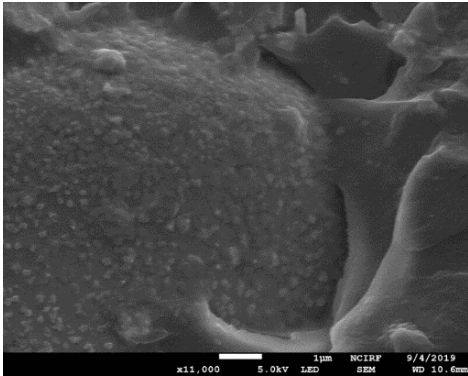


120 kHz

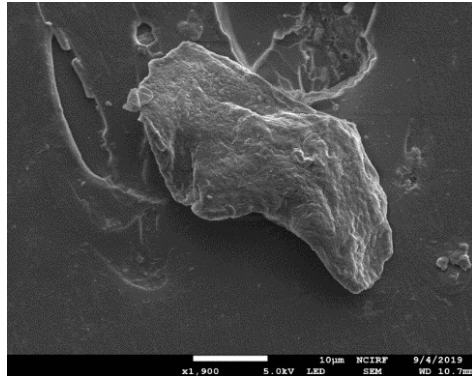


200 kHz

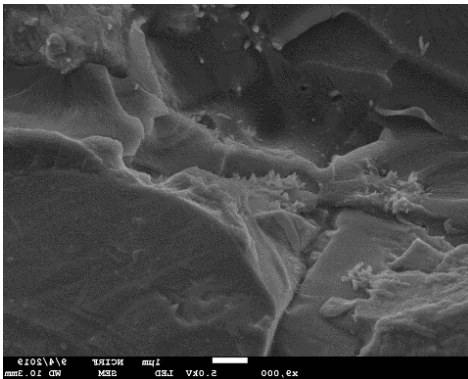
SEM images of cryogenic treated specimens.



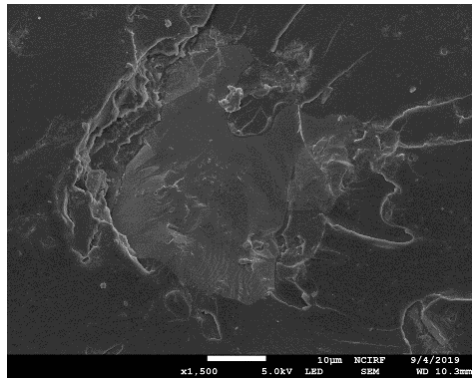
0 kHz



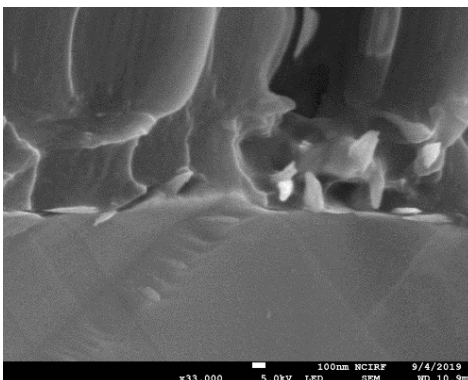
0 kHz



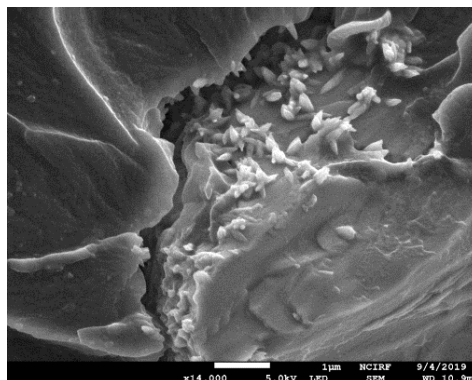
40 kHz



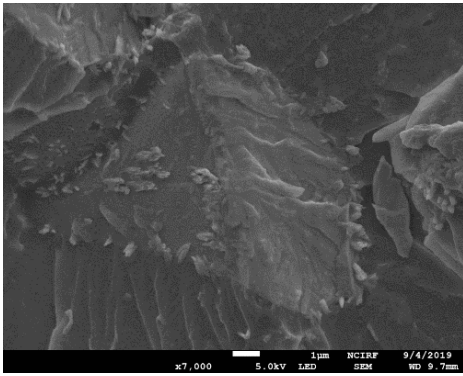
40 kHz



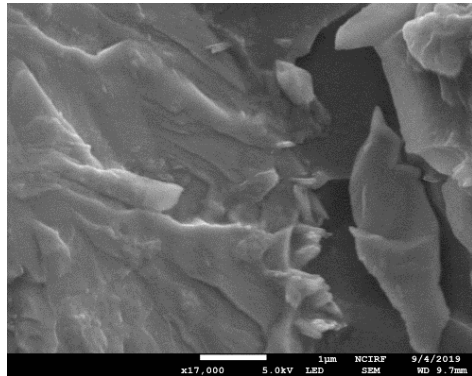
120 kHz



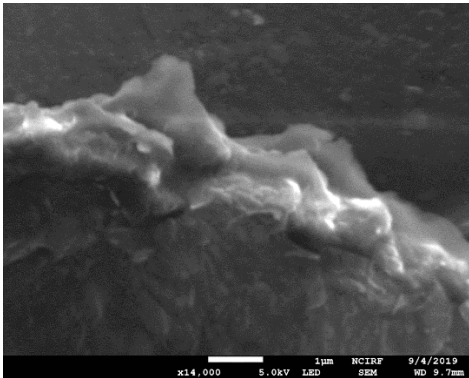
120 kHz



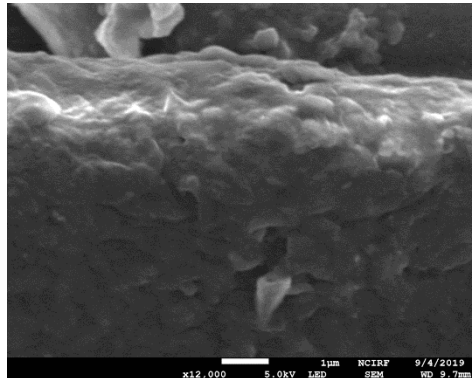
200 kHz



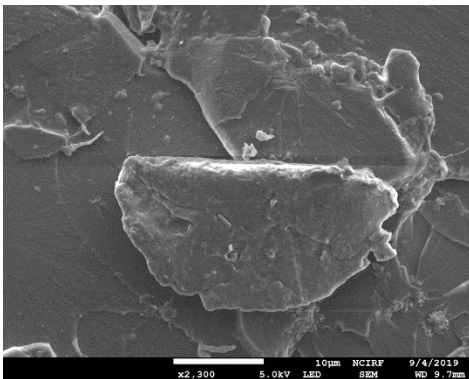
200 kHz



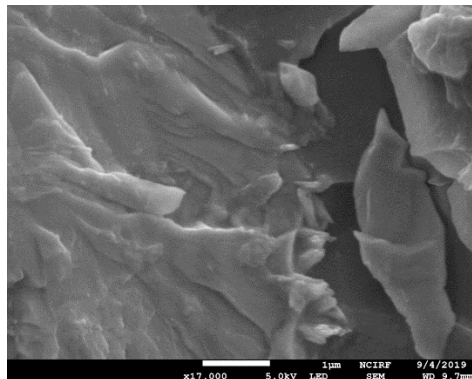
200 kHz



200 kHz

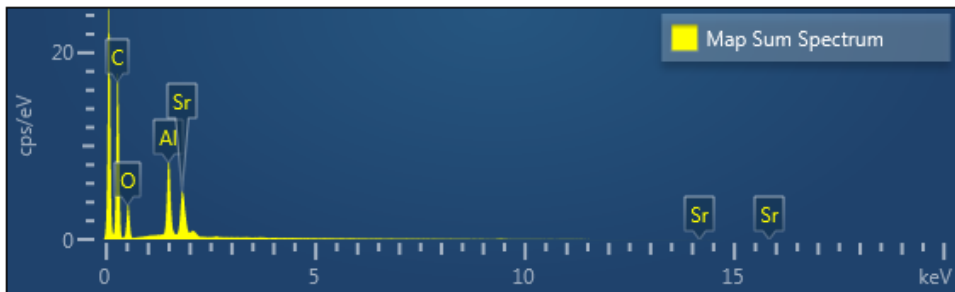
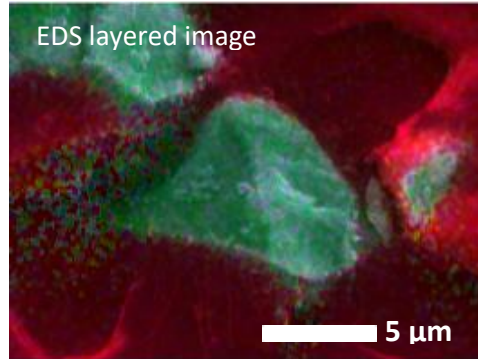
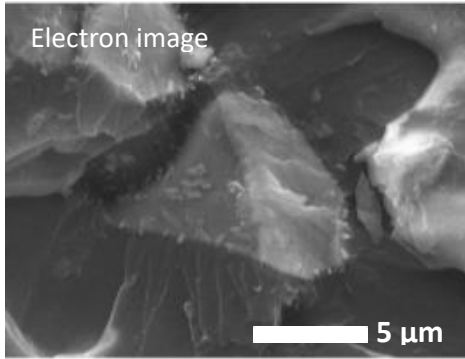


200 kHz

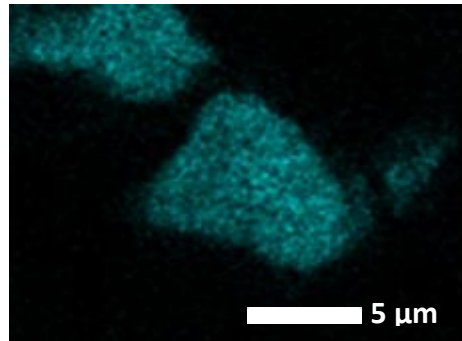
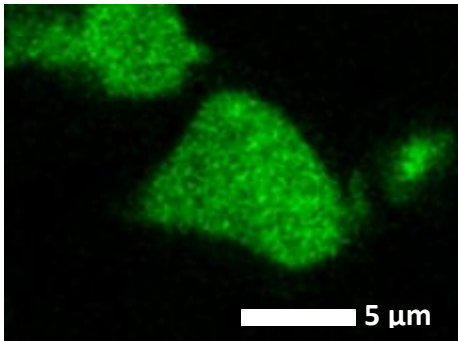
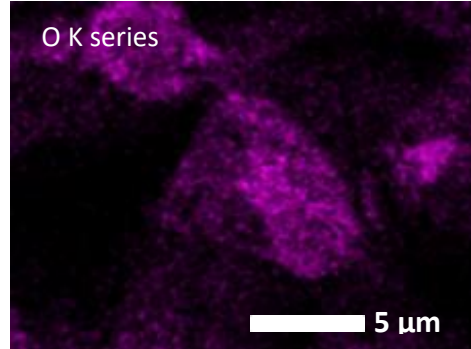
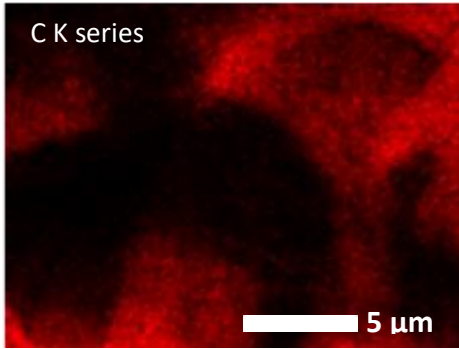


200 kHz

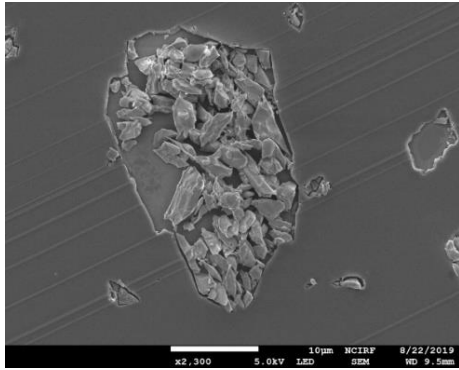
EDS report of cryogenic treated specimens.



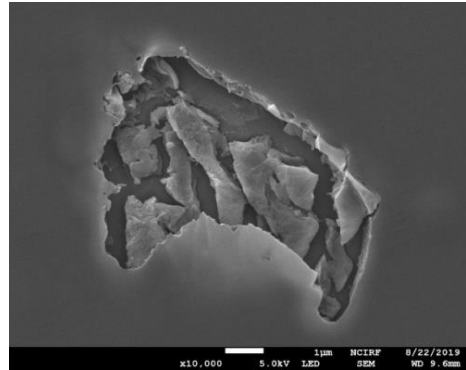
Element	Line Type	Apparent Concentration	k Ratio	Wt%	Wt% Sigma	Standard Label	Factory Standard	Standard Calibration Date
C	K series	2.87	0.02865	67.72	0.20	C Vit	Yes	
O	K series	1.04	0.00350	16.28	0.18	SiO2	Yes	
Al	K series	0.86	0.00615	6.60	0.06	Al2O3	Yes	
Sr	L series	0.99	0.00874	9.39	0.11	SrF2	Yes	
Total:				100.00				



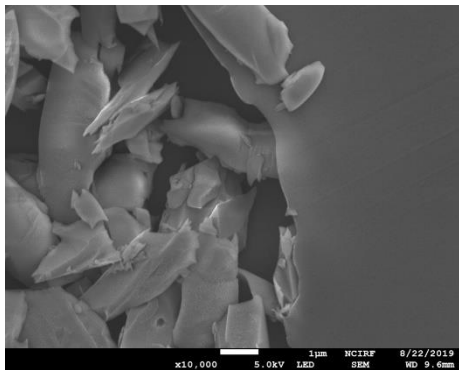
SEM images of microtome treated specimens.



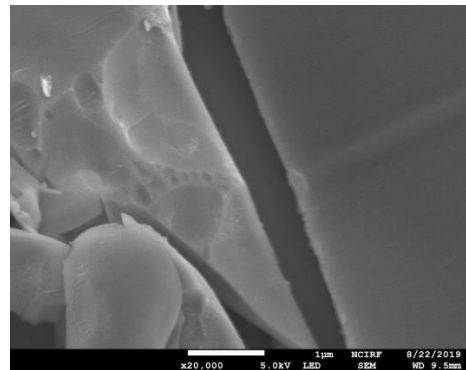
0 kHz



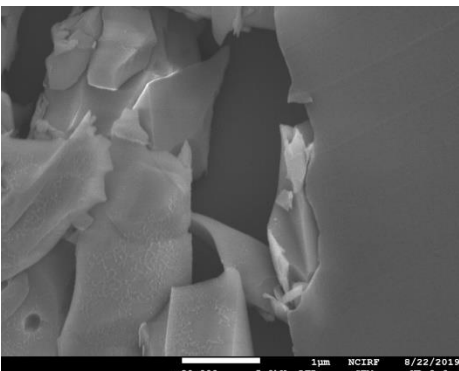
0 kHz



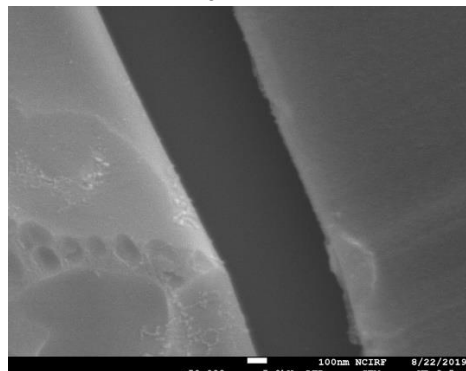
0 kHz



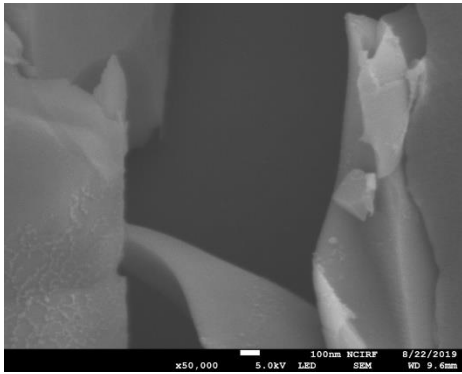
0 kHz



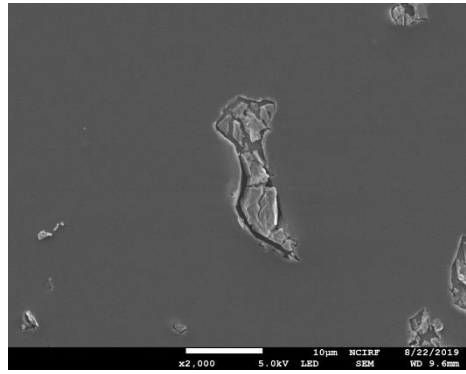
0 kHz



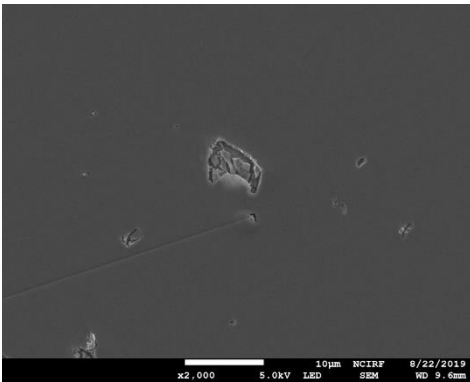
0 kHz



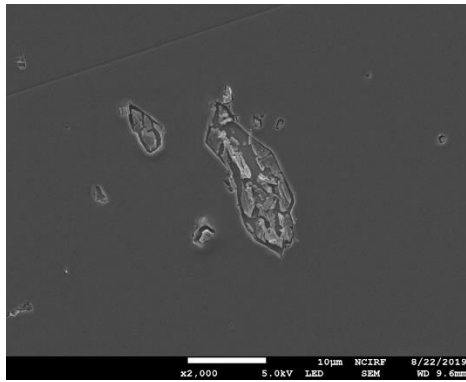
0 kHz



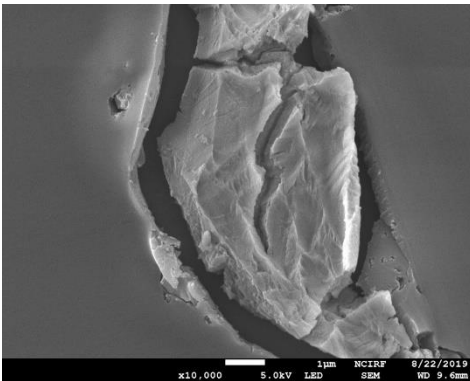
0 kHz



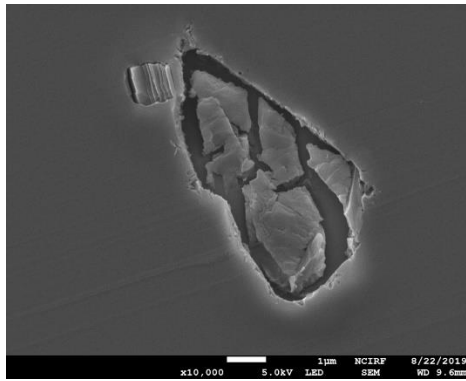
0 kHz



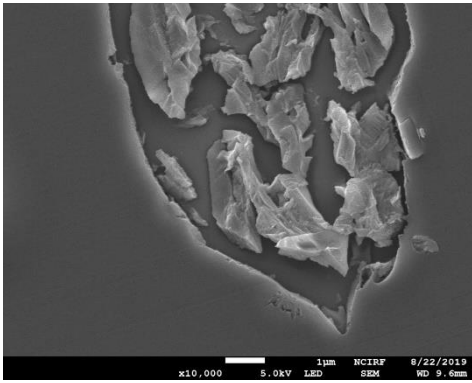
0 kHz



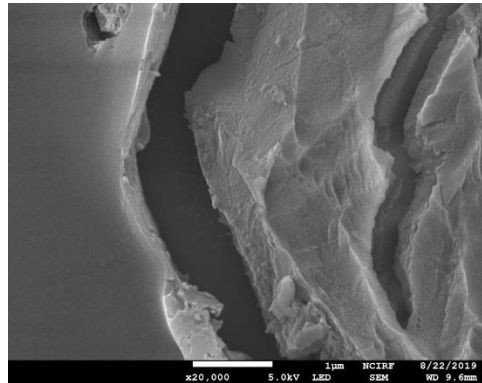
0 kHz



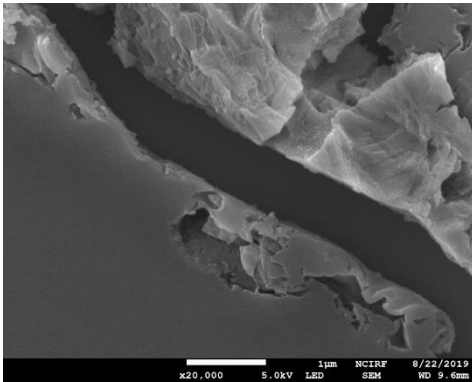
0 kHz



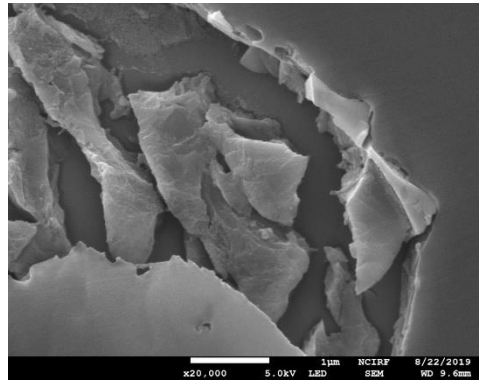
0 kHz



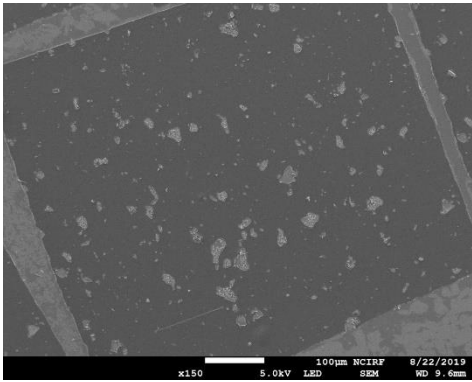
0 kHz



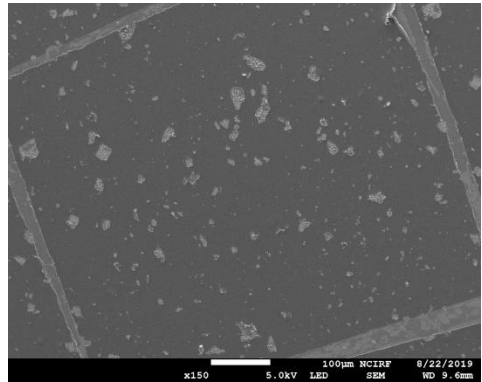
0 kHz



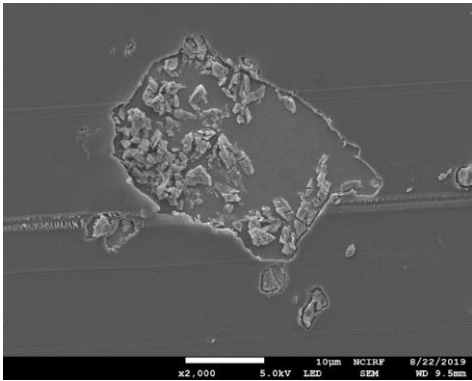
0 kHz



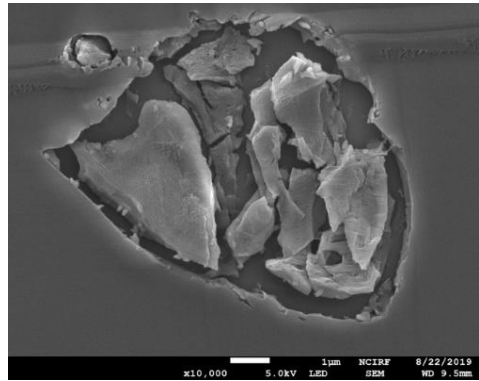
0 kHz



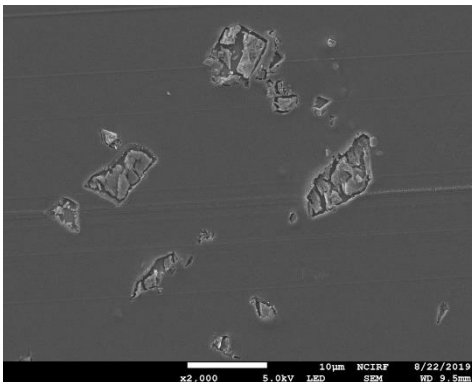
0 kHz



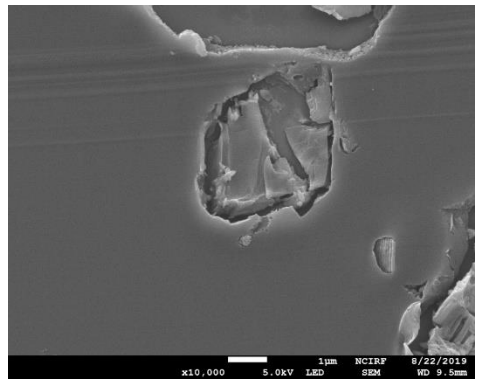
40 kHz



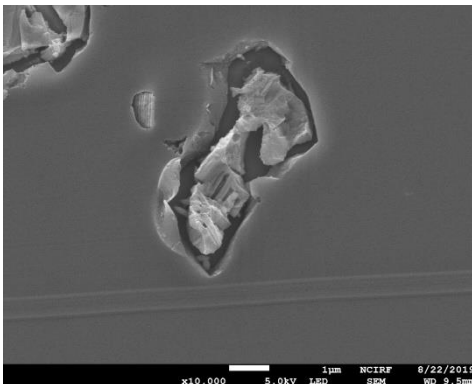
40 kHz



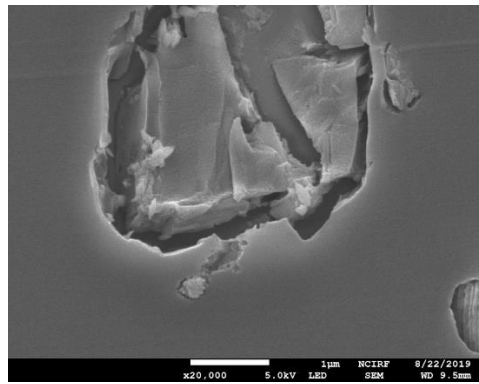
40 kHz



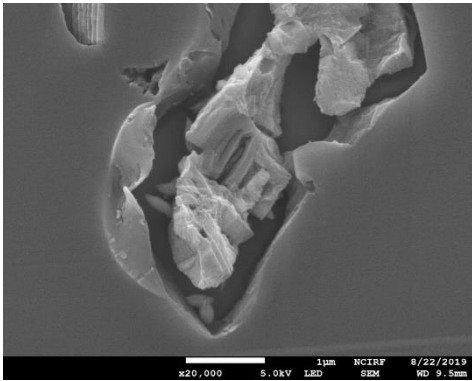
40 kHz



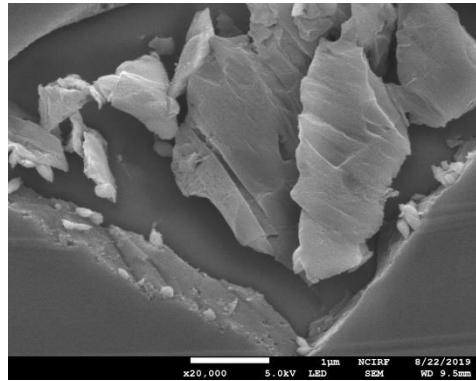
40 kHz



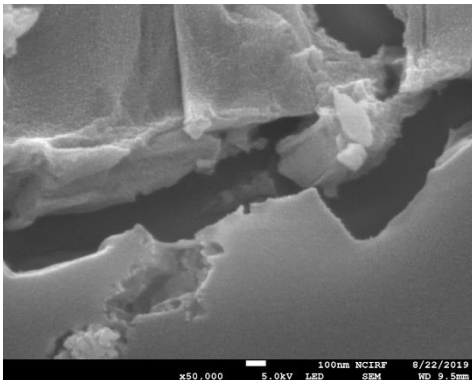
40 kHz



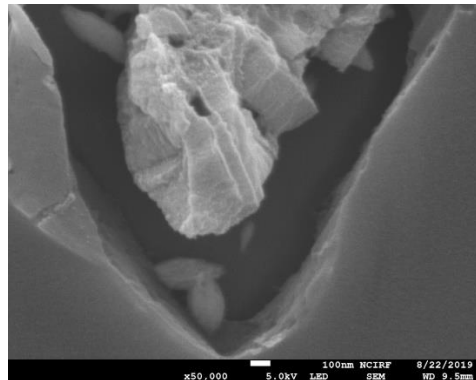
40 kHz



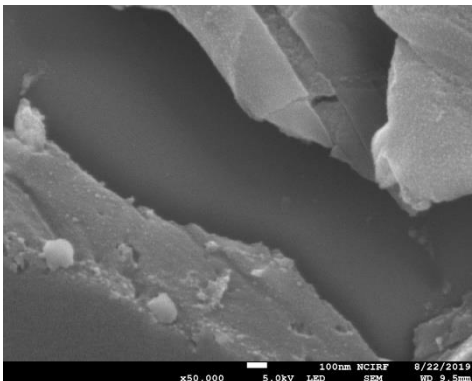
40 kHz



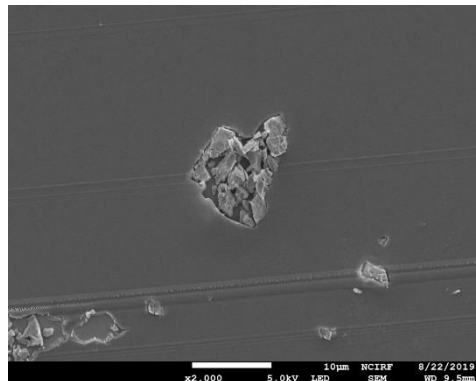
40 kHz



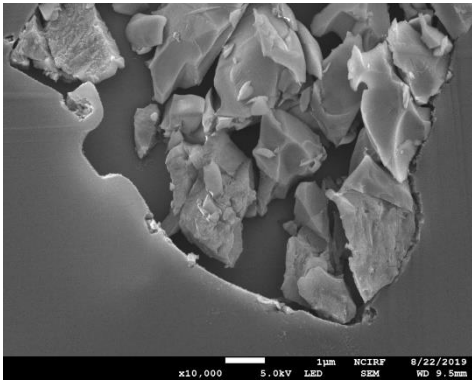
40 kHz



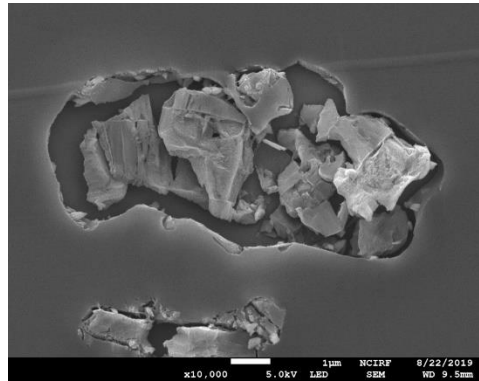
40 kHz



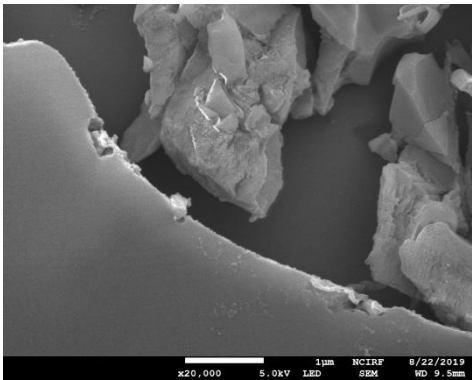
40 kHz



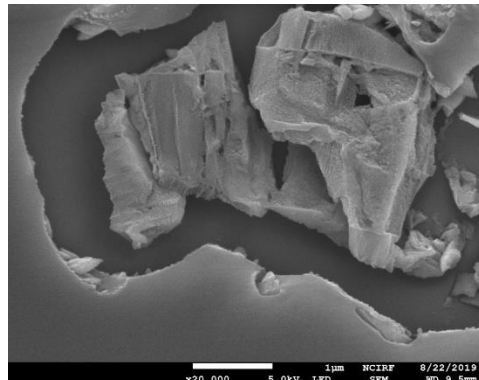
40 kHz



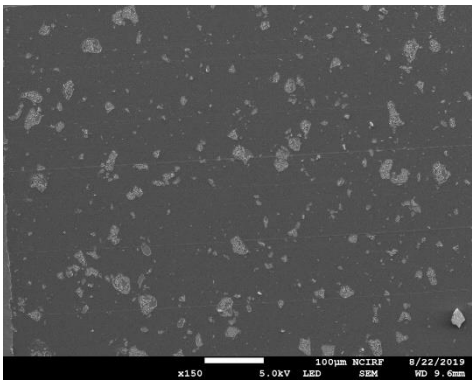
40 kHz



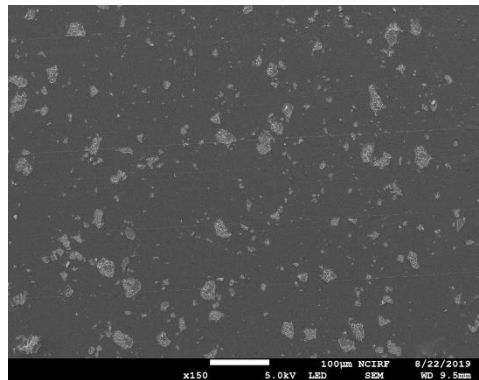
40 kHz



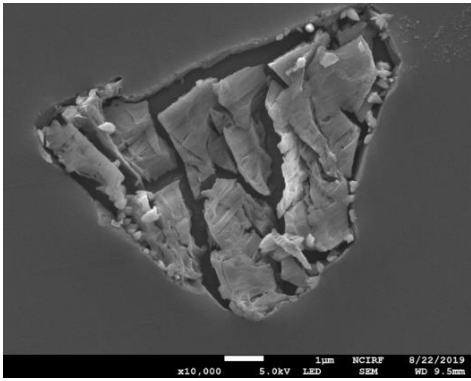
40 kHz



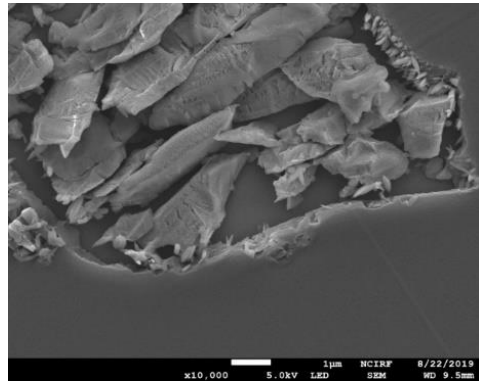
40 kHz



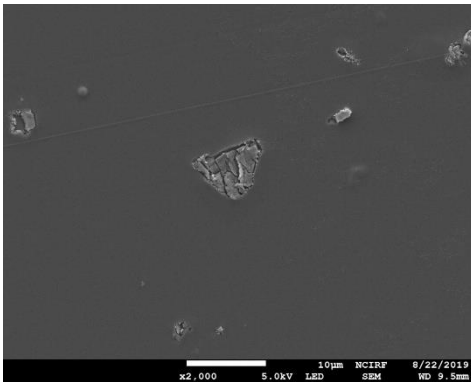
40 kHz



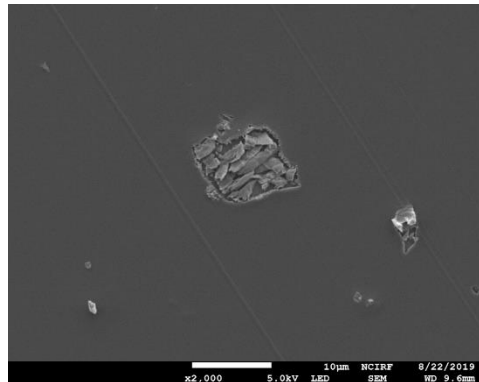
120 kHz



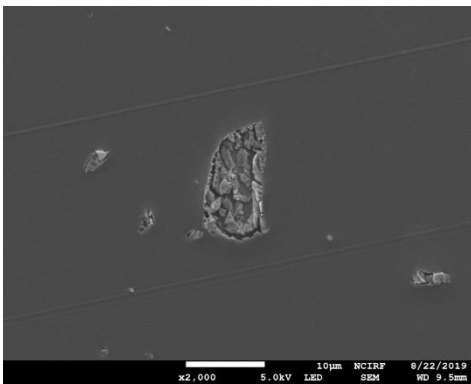
120 kHz



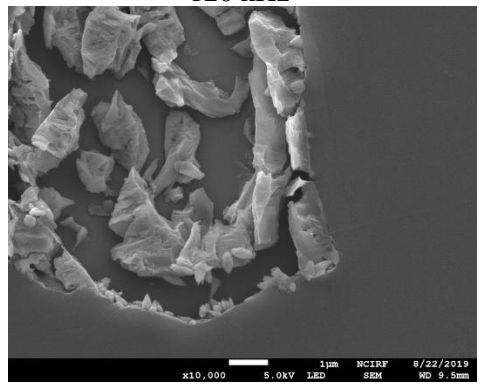
120 kHz



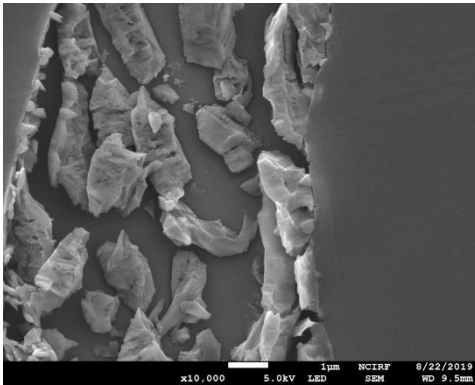
120 kHz



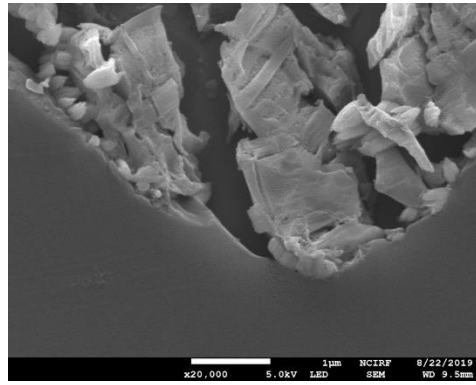
120 kHz



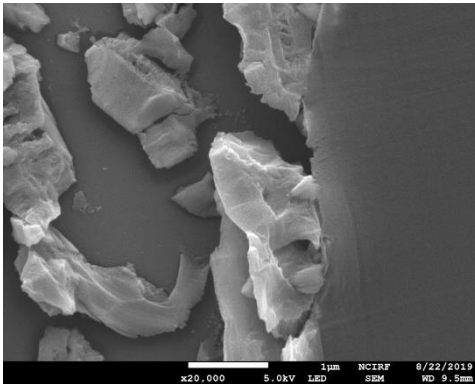
120 kHz



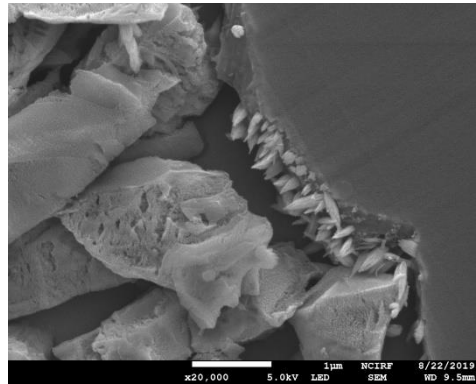
120 kHz



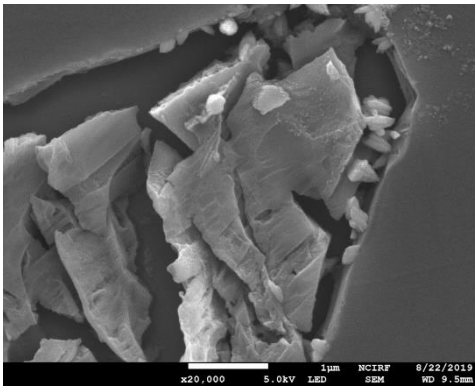
120 kHz



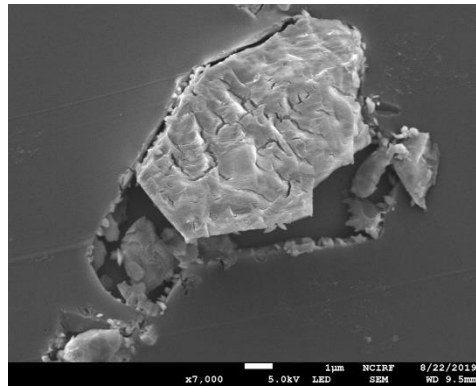
120 kHz



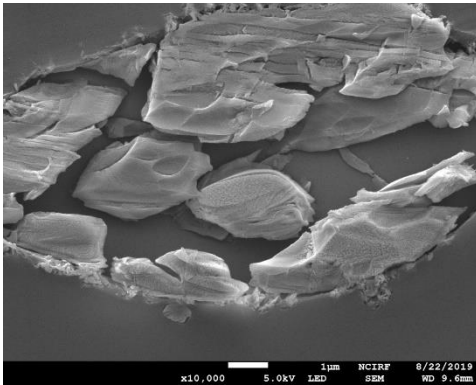
120 kHz



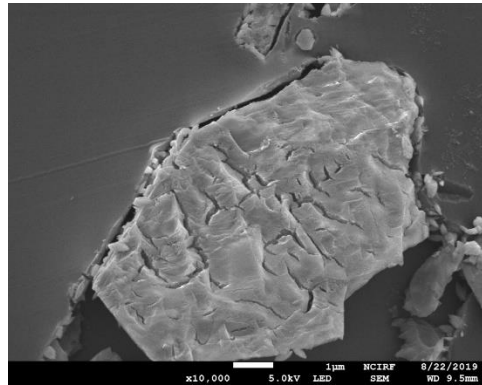
120 kHz



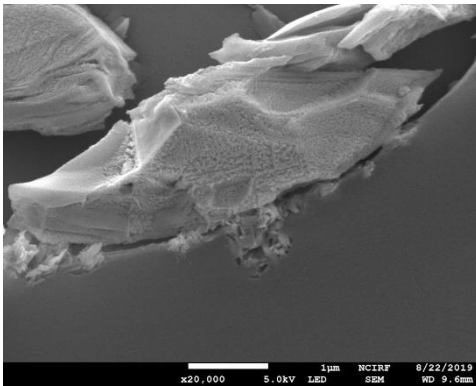
120 kHz



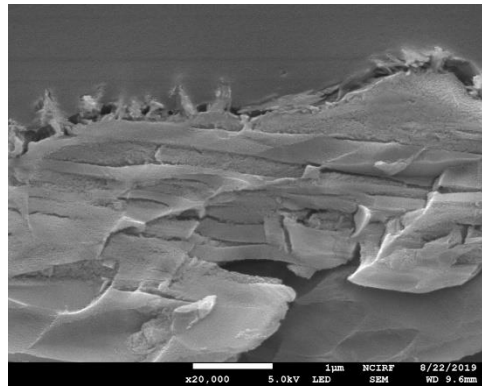
120 kHz



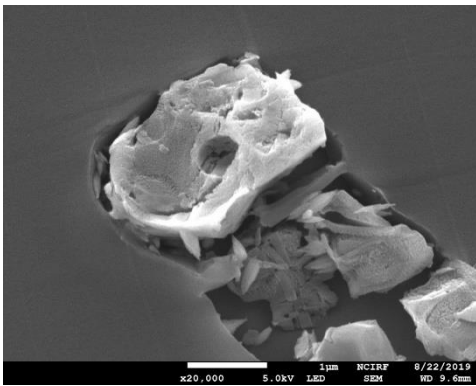
120 kHz



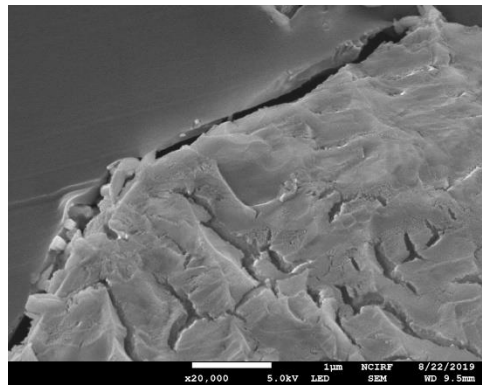
120 kHz



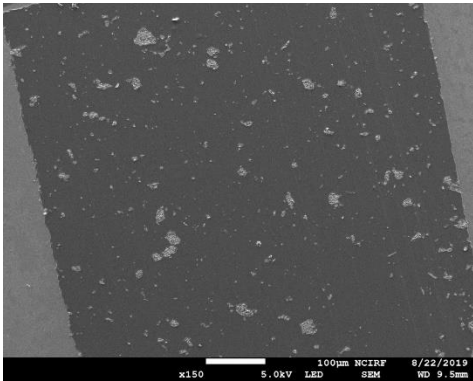
120 kHz



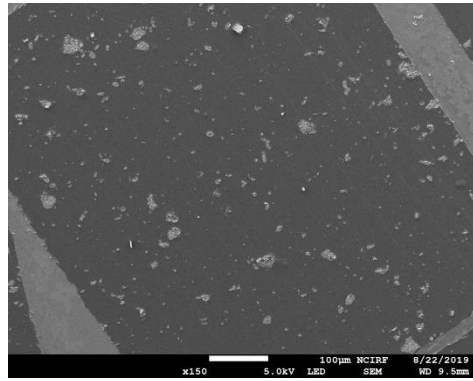
120 kHz



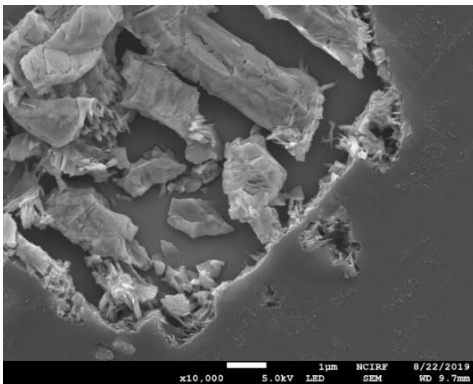
120 kHz



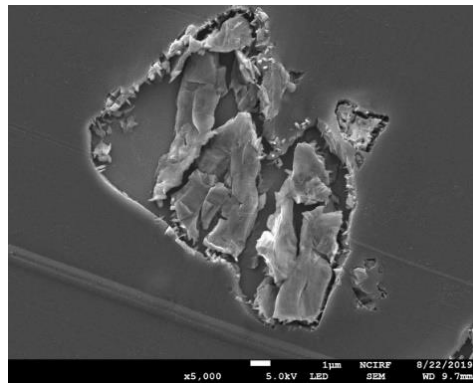
120 kHz



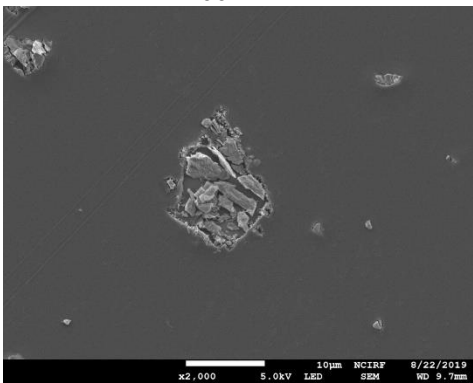
120 kHz



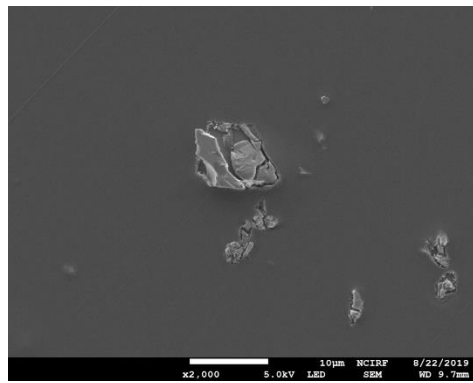
200 kHz



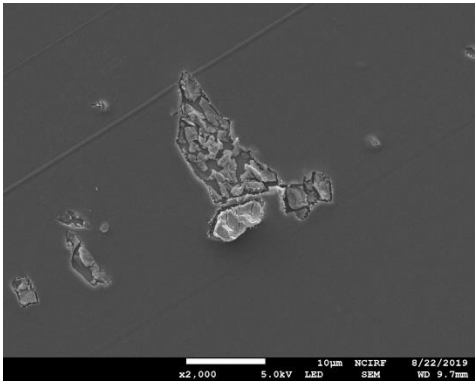
200 kHz



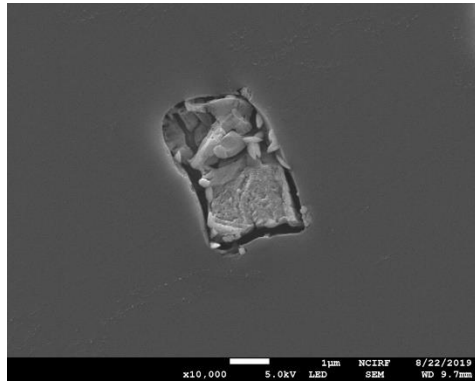
200 kHz



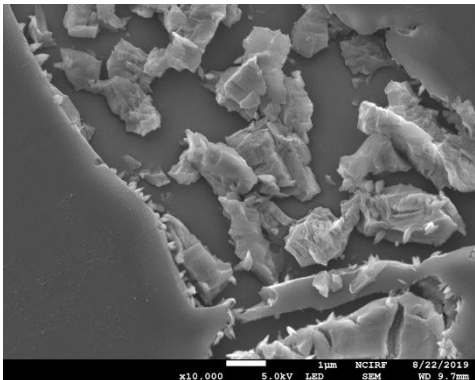
200 kHz



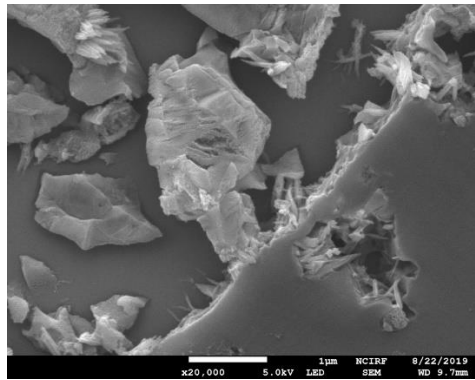
200 kHz



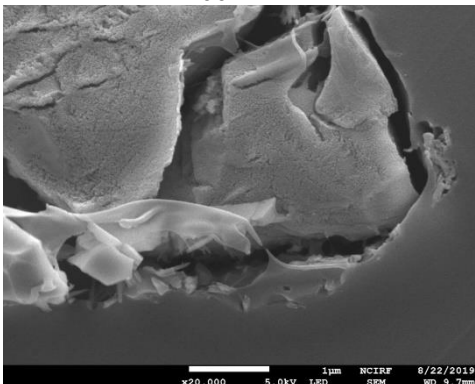
200 kHz



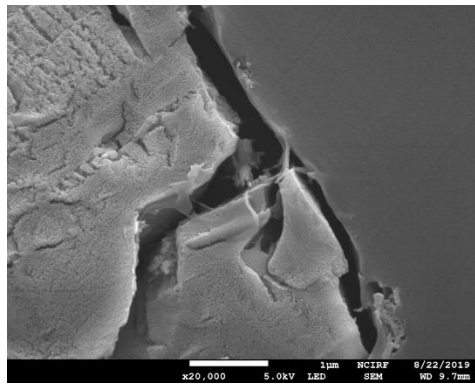
200 kHz



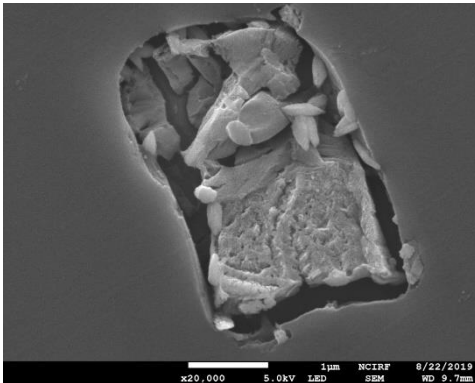
200 kHz



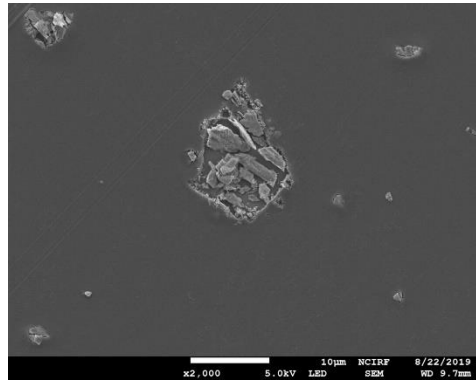
200 kHz



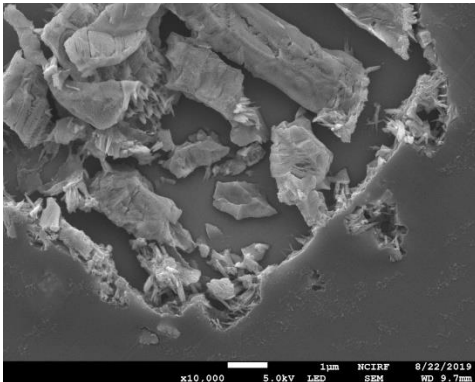
200 kHz



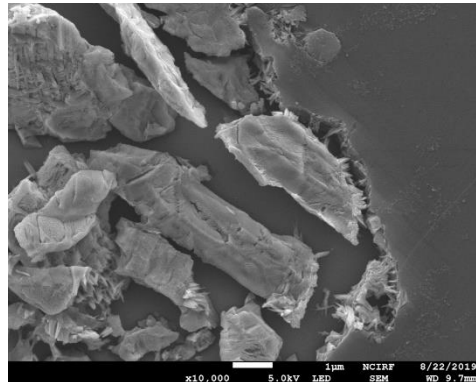
200 kHz



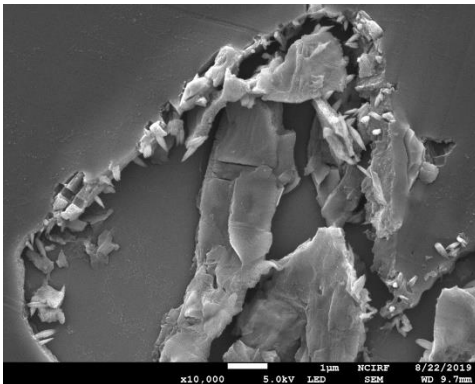
200 kHz



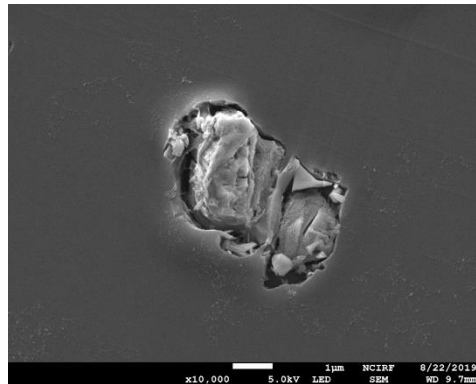
200 kHz



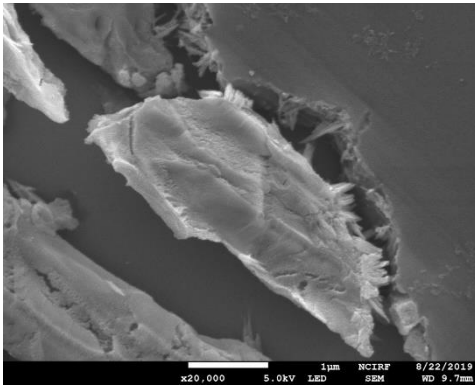
200 kHz



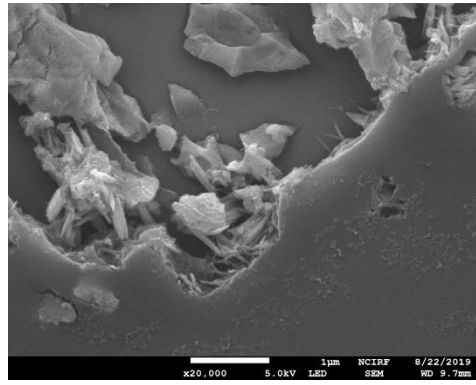
200 kHz



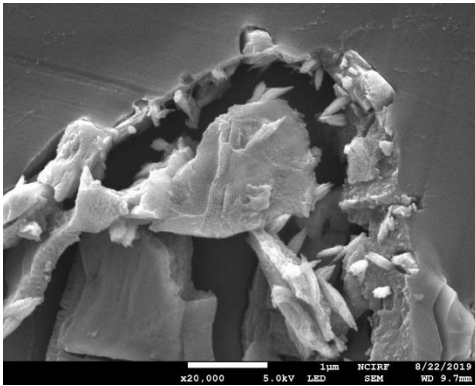
200 kHz



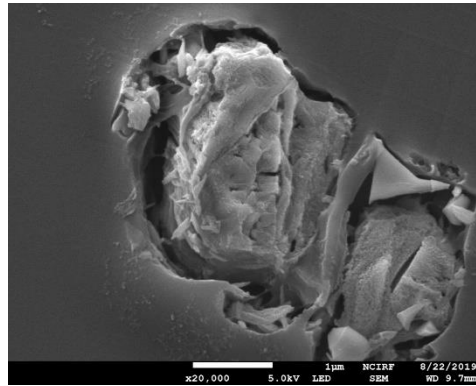
200 kHz



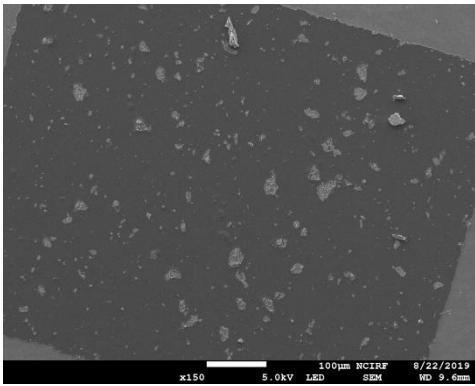
200 kHz



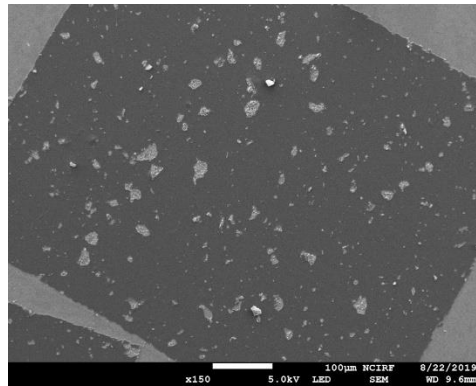
200 kHz



200 kHz



200 kHz



200 kHz

Appendix D. Materials and equipment



Transparent epoxy resin and hardener.



M size SAOED powder at simple view.



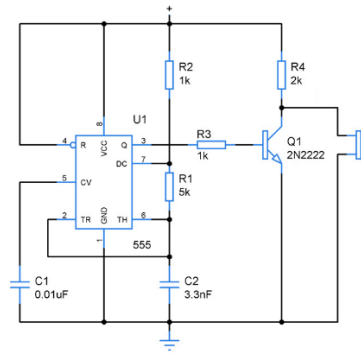
Silicone mold.



Multy-frequency ultrasonic generator 40 kHz, 80 kHz and 120 kHz.



Single high frequency ultrasonic generator 200 kHz.



Homemade ultrasonic generator 40 kHz.



40 kHz ultrasonic transducer.



120 kHz ultrasonic transducer.



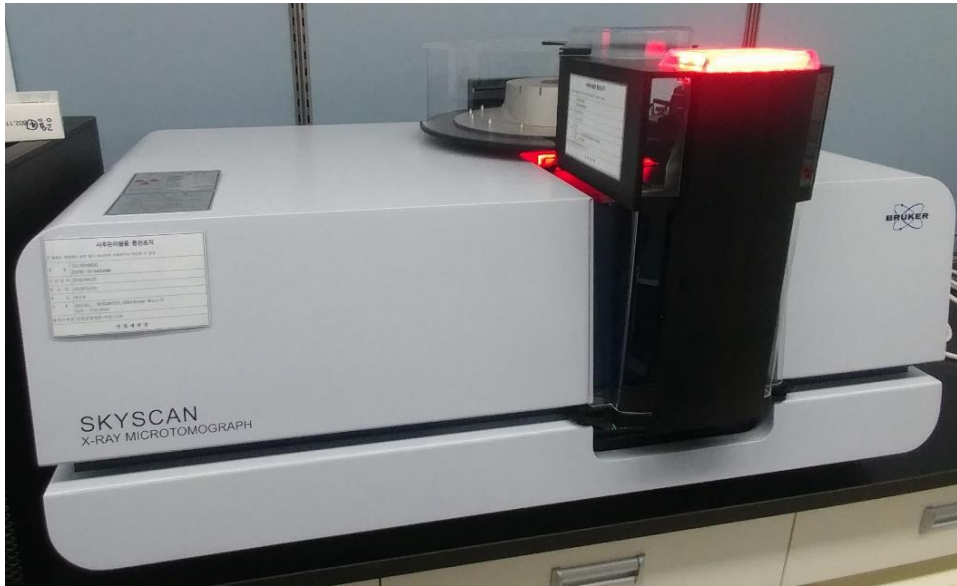
200 kHz ultrasonic transducer.



Sputter Coater 108auto Cressington®.



Field-emission scanning electron microscope JSM-7800F Prime, Supra 55VP.



Micro-CT scanner Skyscan 1275®.



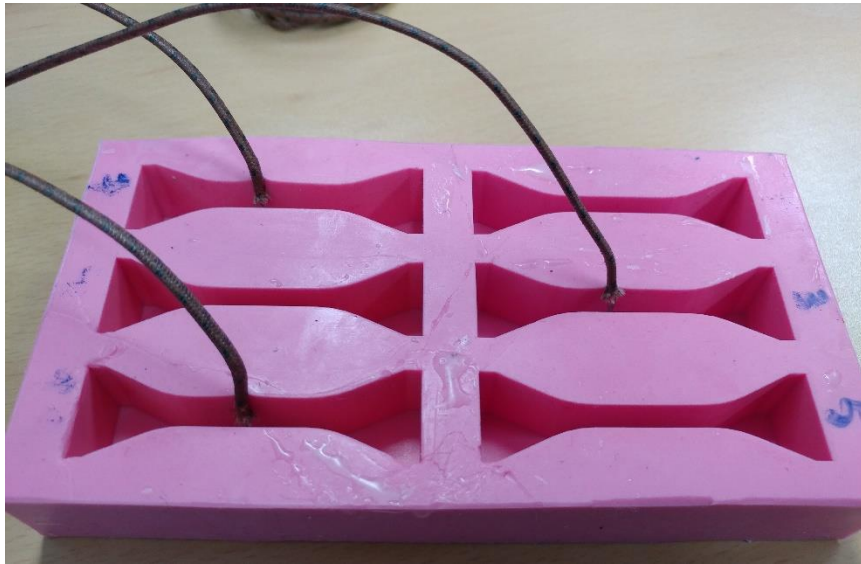
cDAQ 9171 Compact DAQ Chassis.



NI-9213 C Series Temperature Input Module.



J- Type 482 °C thermocouple.



Thermocouples inside silicone mold.

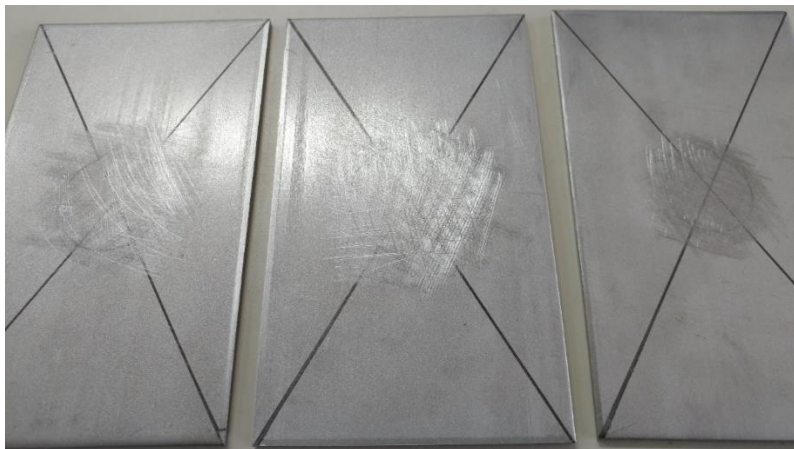


Thermocouples embedded inside cured epoxy/SAOED specimen.

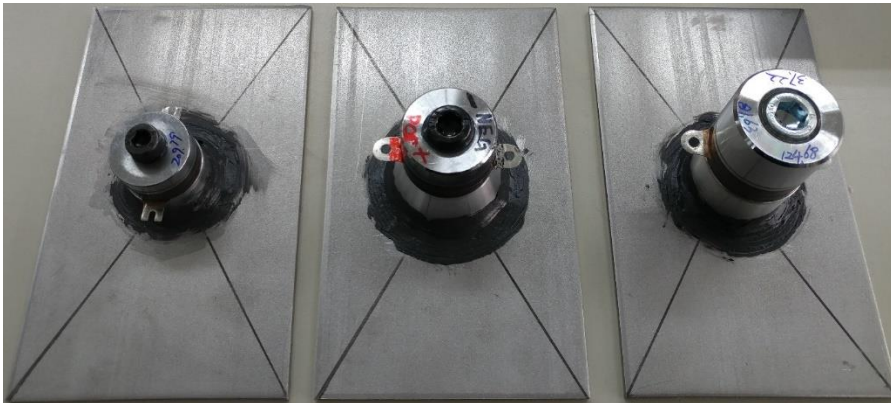
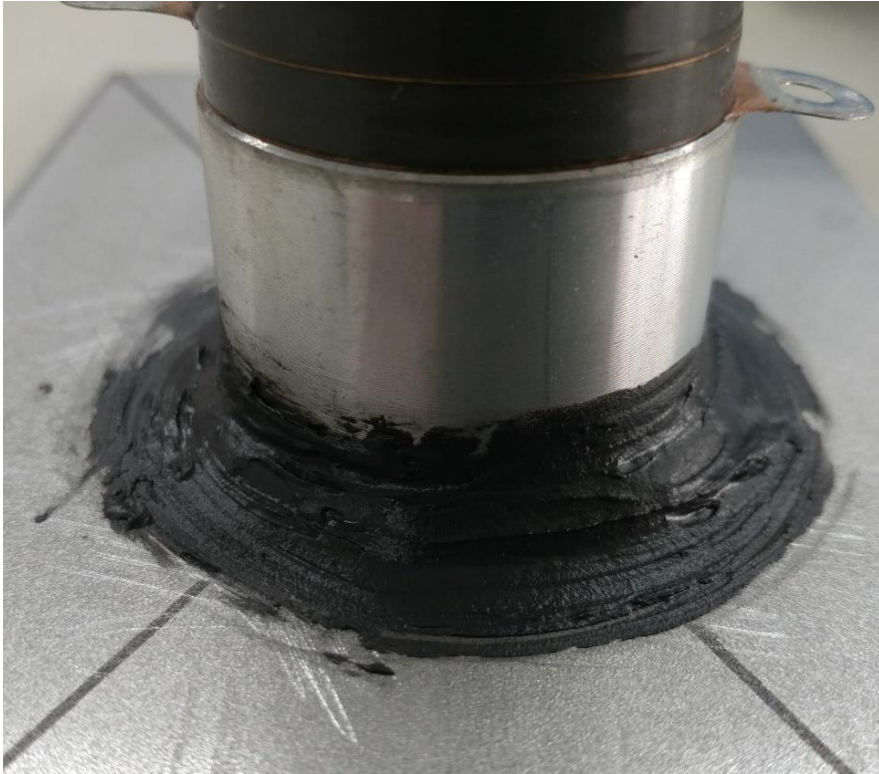
Appendix C. UCT system assembly



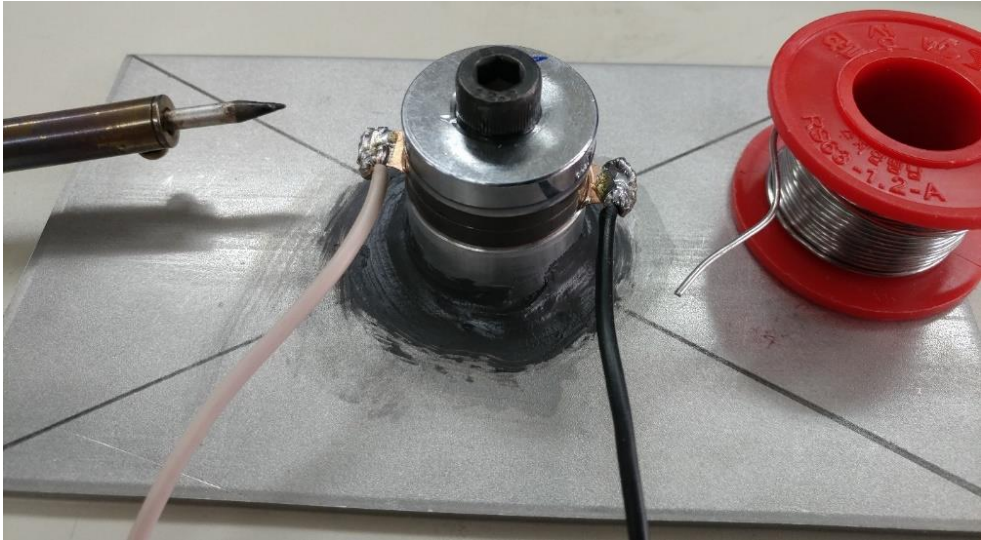
JB Weld®, ultrasonic transducers and metal sheets prior to bonding.



Metal sheets surface was roughen to improve the bonding efficiency.



ultrasonic transducers strongly bonded to the metal sheet.



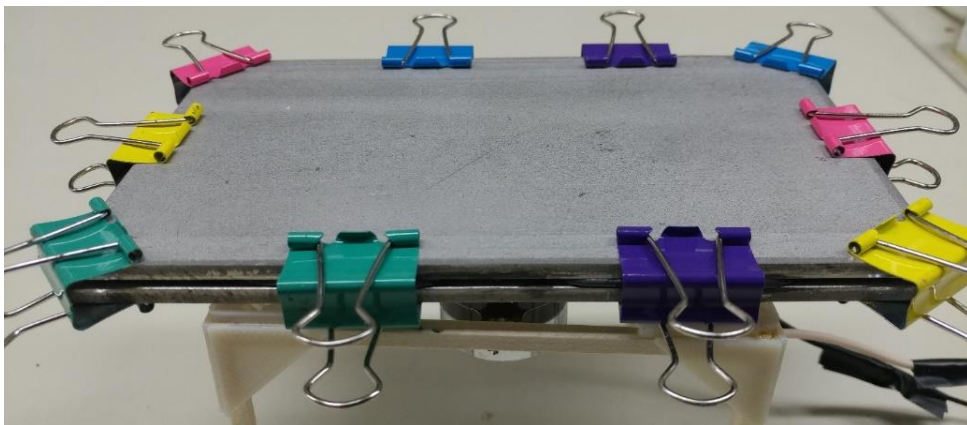
Tin soldering the terminals. Positive (+) WHITE cable. Negative (-) is BLACK cable.



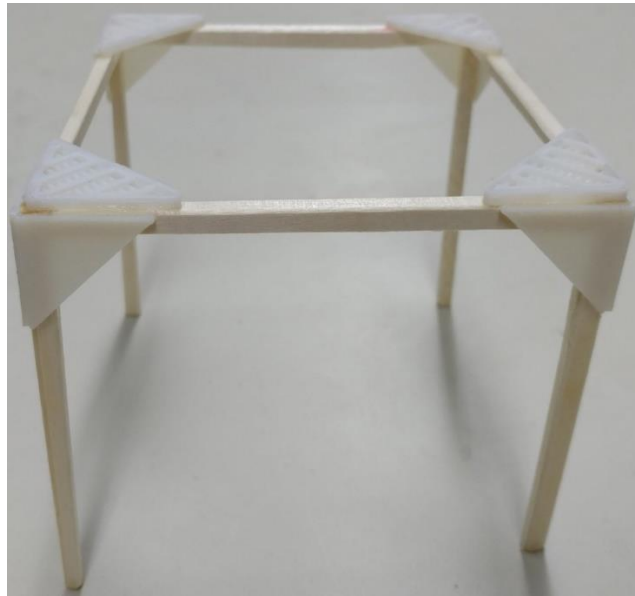
Paper clips of 1 mm thickness are used as separator for the metal sheets.



JB Weld® adhesive is applied in both metal sheets in the specific points where the bond is meant to be.



Metal sheets are clamped together for the JB Weld to cure.



Supports made of 3D printed angles and wood sticks.